Atomic-Scale Evidence for Potential Barriers and Strong Carrier Scattering at Graphene Grain Boundaries: A Scanning Tunneling Microscopy Study

Justin C. Koepke,[†,‡,*] Joshua D. Wood,[†,‡,§] David Estrada,[†,§] Zhun-Yong Ong,[§,⊥] Kevin T. He,[†,‡] Eric Pop,[†,‡,§] and Joseph W. Lyding[†,‡,§,*]

[†]Department of Electrical & Computer Engineering, [‡]Beckman Institute for Advanced Science and Technology, [§]Micro & Nanotechnology Lab, and [⊥]Department of Physics, University of Illinois, Urbana—Champaign, Illinois 61801, United States

ABSTRACT We use scanning tunneling microscopy and spectroscopy to examine the electronic nature of grain boundaries (GBs) in polycrystalline graphene grown by chemical vapor deposition (CVD) on Cu foil and transferred to SiO_2 substrates. We find no preferential orientation angle between grains, and the GBs are continuous across graphene wrinkles and SiO_2 topography. Scanning tunneling spectroscopy shows enhanced empty states tunneling conductance for most of the GBs and a shift toward more n-type behavior compared to the bulk of the graphene. We also observe standing wave patterns adjacent to GBs propagating in a zigzag direction with a decay length of ~1 nm. Fourier analysis of these patterns indicates that backscattering and intervalley scattering are the dominant mechanisms responsible for the mobility reduction in the presence of GBs in CVD-grown graphene.

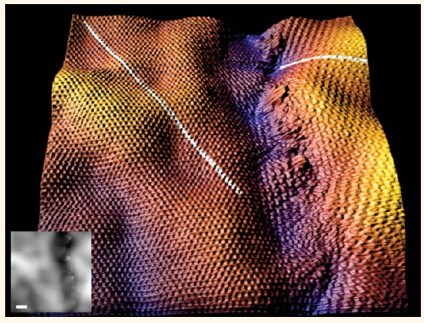

KEYWORDS: graphene · CVD · grain boundaries · scanning tunneling microscopy · spectroscopy · scattering

Graphene is a two-dimensional, zero band gap semimetal with exceptional electrical properties.[1] Wafer-scale growth of monocrystalline graphene with a controllable number of layers is a primary challenge to integrating graphene into nanoelectronic devices and circuits which exploit these properties. Therefore, many researchers are investigating large-scale graphene synthesis by thermal decomposition of Si from SiC(0001)[2] surfaces and transfer to other substrates,[3] as well as by chemical vapor deposition (CVD) on noble and transition metal substrates.[4−8] Among these, CVD growth of graphene on Cu is interesting due to the ability to grow predominantly monolayer graphene[6] and transfer it to other substrates. Since graphene growth on Cu is not epitaxial, this process leads to the formation of randomly oriented grains with shapes based on hydrogen etching, carbon diffusion, and other growth conditions.[9−13] When these individual graphene grains coalesce into a film, graphene grain boundaries (GBs) form. Recent theoretical studies of GBs[14−16] predict modified electronic structures and transport barriers at certain periodic boundaries. Transmission electron microscopy (TEM) and atomic force microscopy (AFM) studies of graphene GBs show that the resulting GBs are aperiodic[17−19] with differing grain sizes.[20] Recent experiments demonstrate the deleterious effects of GBs on carrier transport,[10,21] and recent reports imaged graphene GBs on Cu(111)[22] and Cu foil.[23] While a recent paper[24] reported scanning tunneling microscopy and spectroscopy (STM/S) data for GBs in graphene grown by CVD on Cu, the study was performed in ambient conditions with the graphene still on the Cu foil growth surface. Direct measurements performed under ultrahigh vacuum (UHV) conditions, and after high-temperature annealing, of the graphene GB electronic structure and carrier scattering from GBs in CVD graphene on insulators such as SiO_2 have not been reported yet.

In this work, we investigate GBs in transferred CVD graphene on SiO_2 using UHV

* Address correspondence to jkoepke@illinois.edu, lyding@illinois.edu.

Received for review May 10, 2012 and accepted December 13, 2012.

Published online December 13, 2012
10.1021/nn302064p

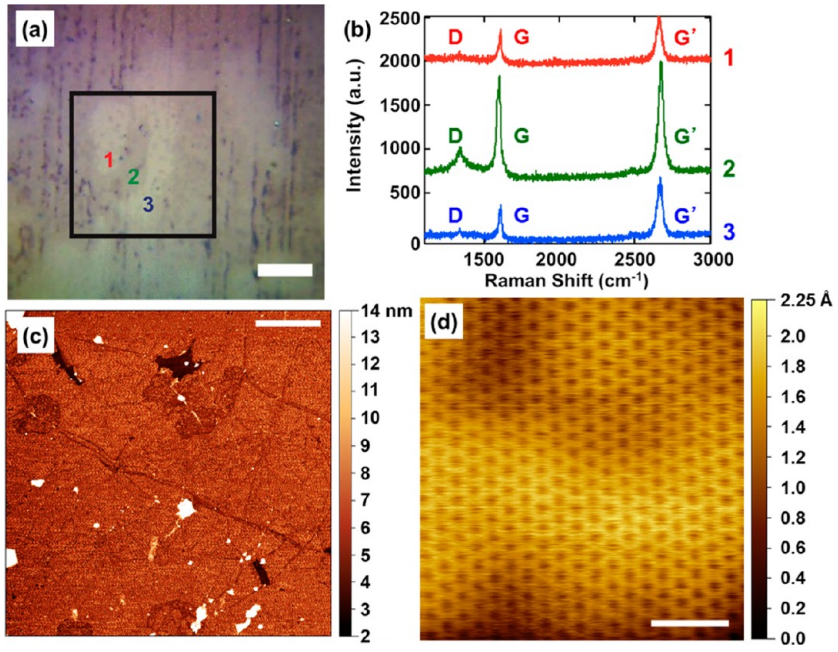

Figure 1. Graphene characterization after growth and transfer to SiO_2/Si. (a) Optical image, with location of Raman spectra indicated and a 5 μm scale bar. Contrast differences indicate regions of monolayer and bilayer graphene. (b) Raman spectra taken at the locations marked in (a) with $I(G')/I(G)$ ratios of 1.05, 1.08, and 1.88 for curves 1, 2, and 3, respectively. The curves are offset for clarity. (c) A 10 μm $\times$ 10 μm tapping mode AFM scan of the graphene sample after cleaning and scanning with the STM, showing some tears in the film and some debris. The scale bar is 2 μm. (d) Small STM scan of the graphene clearly showing the graphene honeycomb lattice. The scale bar is 1 nm.

scanning tunneling microscopy (UHV-STM) and spectroscopy (STS). In agreement with the recent TEM studies of graphene GBs,[17−19] we find that the GBs are aperiodic, as expected from non-epitaxial growth on Cu. We easily distinguish GBs from the growth *versus* wrinkles caused by the growth process[23,25] or induced post-growth by the transfer process.[20,26] The GBs significantly alter the graphene electronic structure, with most showing enhanced empty states tunneling conductance, and lead to localized states at the GBs. Additionally, the local doping of the GBs shifts from p-type in the bulk to lower-doped p-type or n-type doping. We also observe decaying standing waves propagating in the zigzag directions and superstructures immediately adjacent to the GBs. Analyzing these patterns shows a decay length on the order of ~1 nm. Fourier transforms of the STM images show that intervalley scattering and backscattering are the dominant scattering mechanisms from these aperiodic GBs, which lead to the decrease of carrier mobility in CVD-grown graphene.

RESULTS AND DISCUSSION

Figure 1a shows an optical image of our transferred graphene sample on SiO_2/Si. The sample displays areas of differing contrast, which we attribute to multiple graphene layers. Figure 1b gives point Raman spectra taken at the locations marked in Figure 1a, indicating definite variation in the G′/G (also called 2D/G) peak intensity ratio. The ratio for curves 1, 2, and 3 are 1.05, 1.08, and 1.88, respectively. On the basis of the optical contrast and the G′/G intensity ratios, spectrum 1 is near a monolayer and bilayer graphene transition,[27] spectrum 2 is bilayer graphene, and spectrum 3 is monolayer graphene. Thus, the Raman data and the optical contrast show that the growth yielded a mixture of monolayer and bilayer graphene. High-resolution STM scans of the sample reveal that the growth parameters yielded predominantly turbostratic graphene (see Supporting Information). Figure 1c shows a 10 $\times$ 10 μm AFM scan of the graphene after transfer to the SiO_2/Si substrate and surface preparation (*i.e.*, degas at 600−700 °C for 24 h) for the UHV-STM system (see Methods). Clearly, there is debris remaining from the graphene growth or transfer process that was not removed during the sample preparation. The surface also displays graphene film ripples and wrinkles. The smaller line features on the surface are graphene wrinkles[20,25,26,28] and not GBs, as they are too tall compared to GBs observed by STM. A small-area STM image shown in Figure 1d and taken in a region without wrinkles shows the characteristic graphene honeycomb lattice against the underlying SiO_2 topography.

Unlike prior STM studies of GBs in HOPG,[29,30] the graphene GBs in CVD-grown graphene studied here are generally aperiodic. They also show no preferential misorientation angle between the different graphene domains. Further, we note that these GBs occur in regions of turbostratic bilayer graphene

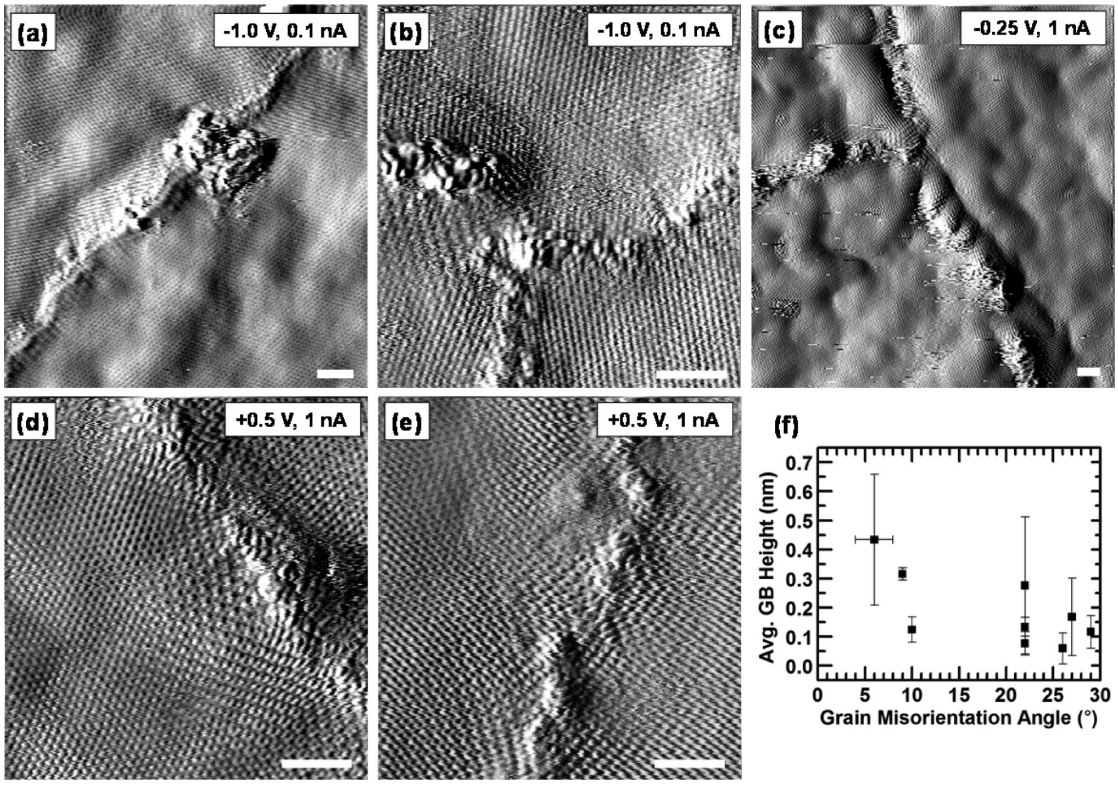

Figure 2. STM images of graphene grain boundaries (GBs). The scale bars are 2 nm. (a) STM image of a GB between two grains misoriented by ~29°. The debris within the scan center is likely remnant PMMA contamination from the graphene transfer. (b) Smaller STM scan of the GBs formed at the meeting point between three different graphene grains misoriented by ~9° (lower left and top), 22° (top and lower right), and 29° (lower left and lower right), respectively. (c) Larger STM scan of a different set of GBs formed at the meeting point between three different graphene grains. The misorientation angles between the grains are ~6° (right and lower left), 20° (lower left and upper left), and 26° (upper left and right), respectively. (d) Smaller STM scan of a GB formed between two grains misoriented by ~27°. Note the very clear $(\sqrt{3} \times \sqrt{3})R30°$ superstructure to the left of the GB. (e) Another GB between two graphene grains misoriented by ~10°. This scan also showed superstructures on both sides of the grain boundary. (f) Plot of average apparent GB height *versus* graphene grain misorientation angle.

(see Supporting Information). Figure 2 shows several GBs, contrast-enhanced by taking spatial derivatives of STM topographs. The misorientation angles between the graphene grains for the GBs shown in Figure 2 are ~6, 9, 10, 20, 22, 26, 27, and 29°. Due to the curvature of the graphene induced by conformation to the underlying SiO_2 surface, there is a mosaic spread of ~1−2° in the measurements. The misorientation angle between the two graphene grains shown in Figure 2a is ~29°, and the resulting GB is well-ordered with the exception of transfer-induced contamination. The triple GB shown in Figure 2b illustrates the difference in disorder and structure of the GBs for three different graphene grain misorientation angles. The misorientation angle between the lower left and upper graphene grains is ~9°, the upper and lower right grains is ~22°, and the lower right and lower left grains is ~29°, respectively. Figure 2c shows another triple GB with misorientation angles between the right and lower left, lower left and upper left, and upper left and right graphene grains of ~6, 20, and 26°, respectively. The GBs shown in Figure 2d,e have relative misorientation angles of ~27 and ~10°, respectively. These images also have $(\sqrt{3} \times \sqrt{3})R30°$ superstructures on both sides of the GBs in each image. The comparison of the heights of the different GBs studied with grain misorientation angle displayed in Figure 2f shows that most of the GBs are around 1−2 Å tall with the GBs with smaller misorientation angles generally having larger and more varied apparent heights in the STM. The average value for all of the GBs measured was ~1.9 Å. The apparent height can also vary by a few angstroms even for GBs with very similar grain misorientation angles. The error bar on the first point for the misorientation angle illustrates the variation in the graphene lattice directions due to the graphene conformation to the SiO_2 topography.

While the recent TEM studies of graphene GBs[17−19] resolved the exact structure of some graphene GBs, the GB electronic structure information was absent. Studies of hexagonal graphene grains measuring the resistances of individual GBs[10,21] have demonstrated their impediment to carrier transport. Here, our ultraclean, UHV-STS measurements of GBs in CVD graphene transferred to SiO_2 fill the knowledge gap between the TEM studies and the individual GB device measurements. The GBs described here (Figures 3 and 4) occur in regions of turbostratic graphene (see Supporting

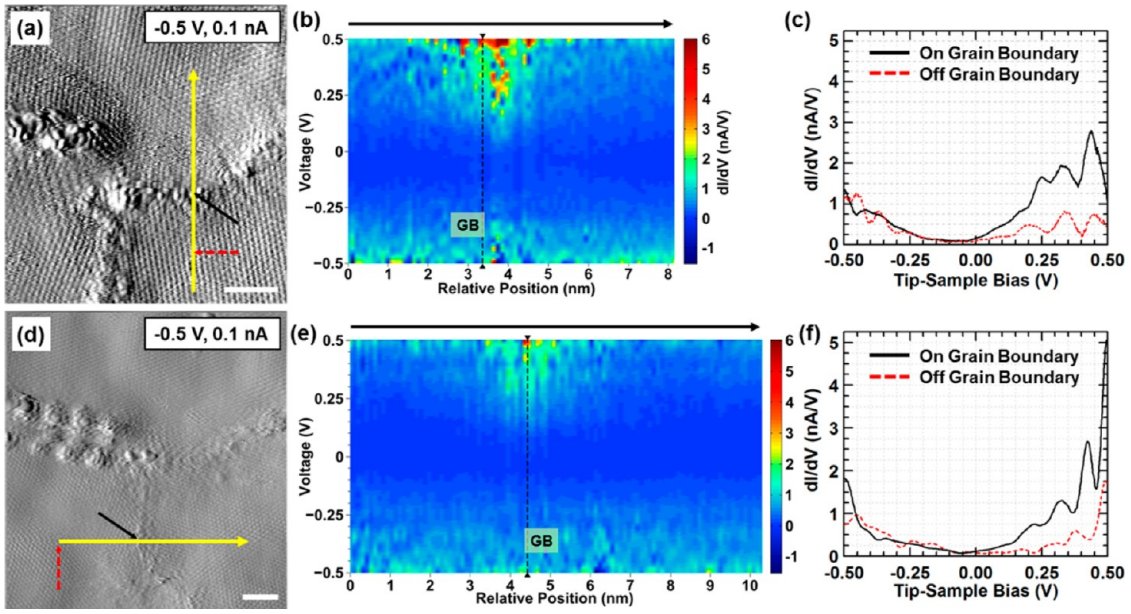

Figure 3. Scanning tunneling spectroscopy (STS) of graphene GBs. (a) STM image of the grain boundaries formed at the meeting point of three graphene grains. The yellow arrow indicates the locations of the spectra. (b) Map of tunneling conductance as a function of tip−sample bias and position from bottom to top of the arrow direction in (a). The vertical, dashed black line indicates the location of the GB. The spectra map shows a marked enhancement of the tunneling conductance in empty states at the GB. (c) Comparison of tunneling conductance for a point on the GB (solid, black line) and a point away from the GB (dashed, red line) to illustrate the enhanced empty states tunneling conductance at the GB. The solid, black and dashed, red arrows in (a) indicate the locations of the respective individual spectra shown in this plot. (d) Larger STM image of the same set of GBs as shown in (a), with the locations of the spectra across the lower GB indicated by a yellow arrow. (e) Map of tunneling conductance as a function of tip−sample bias and position from left to right along the red line shown in (d). The vertical, dashed black line in (e) also indicates the location of the GB. Again, there is a marked enhancement of the empty states tunneling conductance at the GB. (f) Comparison of tunneling conductance for a point on the GB (solid, black line) and a point away from the GB (dashed, red line) illustrating the enhancement seen in (e). The solid, black and dashed, red arrows in (d) indicate the locations of the respective individual spectra shown in this plot. The scale bars in (a) and (d) are 2 nm.

Information). Figure 3a shows the same triple GB from Figure 2b with a yellow arrow indicating the location of a $I-V$ spectra line. The calculated tunneling conductance (dI/dV) spectra map from this spectra line is shown in Figure 3b, with a vertical, dashed black line marking the location of the GB. There is clear enhancement of empty states (dI/dV) between the spectra at and near the GB *versus* that of the graphene further away from the GB. Figure 3c compares individual (dI/dV) spectra taken on (solid, black line) and off (dashed, red line) the GB, showing strong empty states (dI/dV) enhancement at the GB. This asymmetric, enhanced empty states tunneling conductance at the GB is seen in most of the GB spectroscopy studied. Figure 3d shows a larger STM image of the same triple GB as in Figures 2b and 3a with lower resolution than in Figure 3a. The yellow arrow in Figure 3d indicates the location of a line of $I-V$ spectra taken across the GB between the lower left and lower right graphene grains. Figure 3e shows the calculated (dI/dV) tunneling conductance map for the GB marked in Figure 3d. A vertical, dashed black line on the map indicates the GB location. Similarly, these data show enhanced empty states (dI/dV) at the GB as compared to the surrounding graphene. Individual spectra in Figure 3f highlight this observation. Constant tip−sample bias cuts of the spectra map from Figure 3e (shown in Supporting Information Figure S4) illustrate the lateral extent of this enhancement of empty states (dI/dV). We extract decay lengths for the enhanced empty states (dI/dV) from the spectra map shown in Figure 3e, giving an average decay length on the order of 1 nm (see Supporting Information Figure S5).

To first order, normalization of the tunneling conductance by the normal conductance, or (dI/dV)/(I/V), should remove the dependence on the transmission coefficient leaving the normalized surface density of states (DOS) plus a background term.[31] Figure 4a shows the (dI/dV) spectra map from Figure 3b after normalizing the data by I/V,[32] with a vertical, dashed black line indicating the GB location. The asymmetric enhancement present in empty states for the tunneling conductance is not present after normalization by I/V. The individual point comparison in Figure 4b shows the (dI/dV)/(I/V) for the same two points as the (dI/dV) comparison in Figure 3c. This point comparison reiterates that the overall, asymmetric enhancement of empty states in the (dI/dV) data at the GB is not present in the normalized data. Figure 4c,d also shows the (dI/dV)/(I/V) spectra map and individual point comparison for the (un-normalized) (dI/dV) data from Figure 3e,f, respectively. Again, the vertical, dashed black line

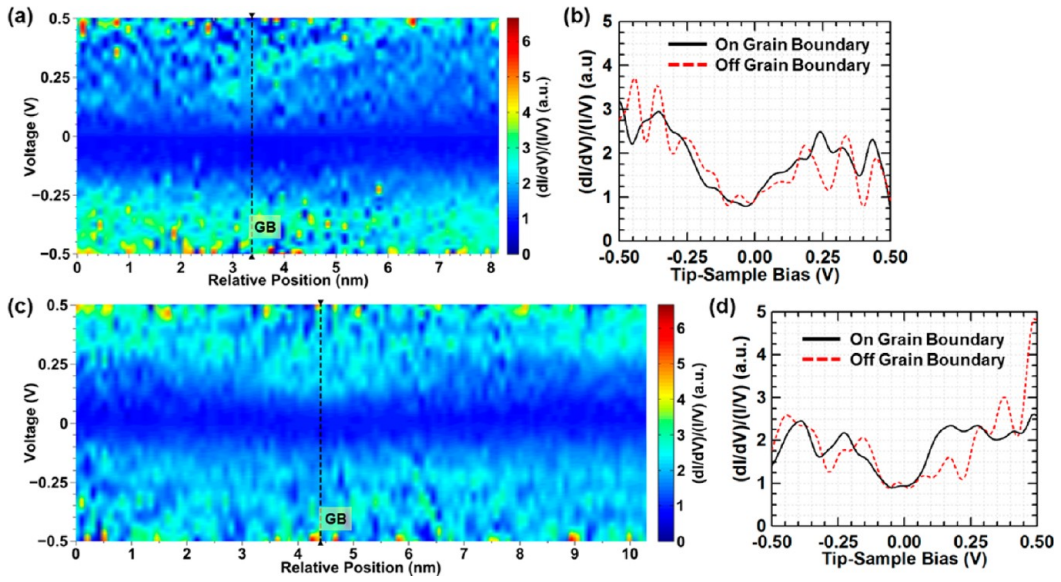

Figure 4. Normalized tunneling conductance of grain boundaries (GBs). (a) Normalized tunneling conductance map for the same spectra as the (non-normalized) tunneling conductance map from Figure 3b. The vertical, dashed black line in (a) indicates the location of the GB. The enhancement seen in empty states for the tunneling conductance data is not present when the data are normalized to the tunneling current. (b) Comparison of the normalized tunneling conductance for a point on the GB (solid, black line) and a point away from the GB (dashed, red line) illustrating the lack of any overall empty states enhancement at the GB. There is a state in (b) at approximately +0.24 V on the GB that is not present away from the GB. (c) Normalized tunneling conductance map for the same data as the (non-normalized) tunneling conductance map from Figure 3e. Here the vertical, dashed black line also indicates the location of the GB. Again, the strong enhancement seen in empty states for the (non-normalized) tunneling conductance data from Figure 3e is not present when the data are normalized to the tunneling current. (d) Normalized tunneling conductance comparison for a point on the GB (solid, black line) and a point away from the GB (dashed, red line). There is no overall enhancement in empty states at the GB as there was for the non-normalized tunneling conductance. However, there is a state at approximately +0.15 V at the GB, which is not present away from it.

indicates the GB location. The normalization of this data also removes the asymmetric, empty states enhancement present at the GB in the (un-normalized) (d*I*/d*V*). The *I*−*V* spectra for both GBs in Figures 3 and 4 also show higher current in empty states on the GBs than on the surrounding graphene. This removal of the enhanced empty states (d*I*/d*V*) present at the GBs upon normalization by *I*/*V* suggests that the asymmetric, enhanced empty states (d*I*/d*V*) at the GBs arises from a tunneling transmission coefficient effect due to a change in apparent barrier height at the GBs. The spectra map in Figure 4c also shows localized states near the GB at approximately +0.15 V that decay away from the GB. The individual (d*I*/d*V*)/(*I*/*V*) point comparison in Figure 4d also shows these states at the GB near +0.15 V that are not present away from the GB. This implies that the states are a local property of this particular GB. The presence of localized states at and near the GB in the data from Figures 4c−d is consistent with observations on periodic GBs in HOPG, whose localized states depend on the GB structure.[29,30] We note that the "oscillations" visible in the individual (d*I*/d*V*) and (d*I*/d*V*)/(*I*/*V*) spectra in Figures 3c, 3f, 4b, and 4d are from noise in the original *I*−*V* spectra from which the (d*I*/d*V*) are calculated and are not from Landau levels caused by strain within the graphene.[33] We also note that our energy resolution is limited by the room-temperature measurements to ∼50 meV, typical for thermal broadening at room temperature in the STM sample and tip.

Since no pronounced secondary minima are present in the (d*I*/d*V*) spectra shown in Figure 3, the minimum of the (d*I*/d*V*) corresponds to the Dirac point.[34] The plot in Figure 5a shows the tip−sample bias of the minimum of the (d*I*/d*V*) spectra from the line of spectra across the GB from Figure 3d, which has a misorientation angle of ∼29° and an average apparent height of 0.12 nm. From the Gaussian fit (red line), the Dirac point on the GB occurs at −0.044 V and the value in the surrounding graphene away from the GB is +0.057 V. We convert these Dirac point values to charge-carrier concentration using the equation $n = (E_D^2)/(\pi\hbar^2 v_F^2)$, where E_D is the energy of the Dirac point, $\hbar$ is Planck's constant divided by 2π, and n is the carrier concentration, and v_F is the Fermi velocity ($v_F = 10^6$ m/s). We note that this is a fair first order estimate of the doping.[15,24,35] This gives a p-type doping of 2.4×10^{11} cm^{-2} in the bulk graphene away from the GB and an n-type doping of 1.4×10^{11} cm^{-2} at the GB. The full width at half-maximum for this doping change from the Gaussian fit is ∼3.6 nm. So the GB from Figure 3d shifts the doping from p-type to n-type, creating a *p*-*n*-*p* junction and changing the local work-function over a distance of ∼3.6 nm.

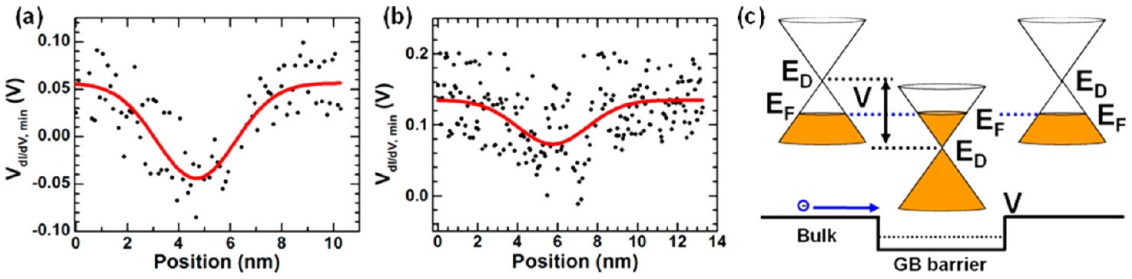

Figure 5. Voltage of (d*I*/d*V*) minimum versus position showing a barrier at the grain boundary. (a) Plot of tip−sample bias (V) of the (d*I*/d*V*) minimum at each point in the line of STS across the GB from Figure 3d. The shift of the minimum here indicates a transition from p-type doping in the bulk to n-type doping at the GB. (b) Plot of tip−sample bias (V) of the minimum of the (d*I*/d*V*) at each point in a line of STS across the GB from Figure 2d also showing a shift toward n-type doping. (c) Diagram illustrating the shift in doping caused by the presence of the GB. This one illustrates a *p-n-p* doping shift.

Similarly, Figure 5b shows the tip−sample bias of the minimum of the spectra from a line of spectra across the GB from Figure 2d. The GB from Figure 2d has a misorientation angle of ∼27° and an average apparent height of 0.17 nm. The Gaussian fit (red line) for this data gives a Dirac point in the bulk graphene away from the GB of +0.13 V and a Dirac point on the GB of +0.073 V. The full width at half-maximum of this Gaussian fit is ∼4.2 nm. These correspond to p-type doping of 1.3×10^{12} cm^{-2} in the bulk graphene away from the GB and p-type doping of 3.9×10^{11} cm^{-2} at the GB. Hence this second GB has *p-p′-p* doping (*p′*<*p*). In both cases, the presence of the GB shifts the doping toward n-type from the bulk, or decreases the work function. This decrease in work function would modify the apparent tunneling barrier height and affect the tunneling transmission coefficient.

Our results show that the modified topological structure of the GBs leads localized states and decreases the work function. Normalization of the (d*I*/d*V*) spectra by *I*/*V* suggests that the observation of enhanced empty states (d*I*/d*V*) at the GBs arises from transmission coefficient change due to a change in apparent tunneling barrier height, as would occur with the measured work function change at the GBs. Supporting Information Figure S6 contains a plot illustrating how a shift in doping, with a decrease in work function, could lead to the observed enhanced empty states (d*I*/d*V*) at the GBs described in Figures 3 and 4. Furthermore, a recent STS study of N-doped CVD graphene also observed enhanced empty states (d*I*/d*V*) near the sites of the dopants compared to the undoped CVD graphene.[36] The Supporting Information contains spectroscopy of GBs in CVD graphene on mica with water trapped between the graphene and the mica.[37] The GBs on this surface, which does not have the same charge puddling as graphene on SiO_2/Si,[38,39] also have doping shifts and potential barriers. Supporting Information Figure S7 shows a large-angle GB with a barrier of ∼0.06 V that shifts the doping from p-type to n-type (see Supporting Information). Depending on the GB topology, the misorientation angle, and the background doping of the bulk graphene, the shift in the work function can lead to the formation of a graphene *p-n-p* junction (Figure 5c), where the transition between the doping levels occurs over a width of ∼1.8−2.1 nm. We note that the length scale for this doping shift associated with the GBs is ∼1−2 nm, while the length scale associated with the doping fluctuations due to charge puddling of graphene on SiO_2/Si is closer to 10−20 nm or more.[38,39]

Spectroscopy of a small-angle GB in a region of monolayer CVD graphene on mica with water trapped between the graphene and the mica (Supporting Information Figure S8) suggests that local states may also play a role in the enhanced empty states (d*I*/d*V*) at the GB. The particular GB in Supporting Information Figure S8 has a very small potential barrier on the order of the thermal voltage, ∼0.026 V, but has slightly higher (d*I*/d*V*) on the GB for both filled and empty states than the surrounding graphene grains. Since there is only a thermally negligible doping shift at the GB, local states at the GB must lead to the symmetric, locally enhanced (d*I*/d*V*). See the Supporting Information and Figures S10 and S11 for spectroscopic data on back-gated graphene GBs on SiO_2/Si.

In addition to topographic and spectroscopic information, the STM can also study carrier scattering in graphene[40,41] by observing electronic superstructures induced by defects, adsorbates, or edges. We achieve this by means of fast Fourier transforms (FFTs) and FFT filtering, which elucidate carrier scattering from the graphene GBs.[40,41] Figure 6a shows a topographic STM image of a GB between two graphene grains misoriented by ∼29°, with the grain to the left of the GB labeled "L" and the grain to the right of the GB labeled "R." The false-colored STM topographic derivative given in Figure 6b provides better contrast of the graphene lattice. From this, a linear superstructure is apparent on both the left and right sides of the GB, and these superstructures propagate in different directions on each side of the GB. The top panel of Figure 6c shows a small section (dashed, cyan box) of the image shown in Figure 6b, taken to the left of the GB, and its resulting 2D FFT, showing the six bright outer points characteristic of the graphene reciprocal lattice.

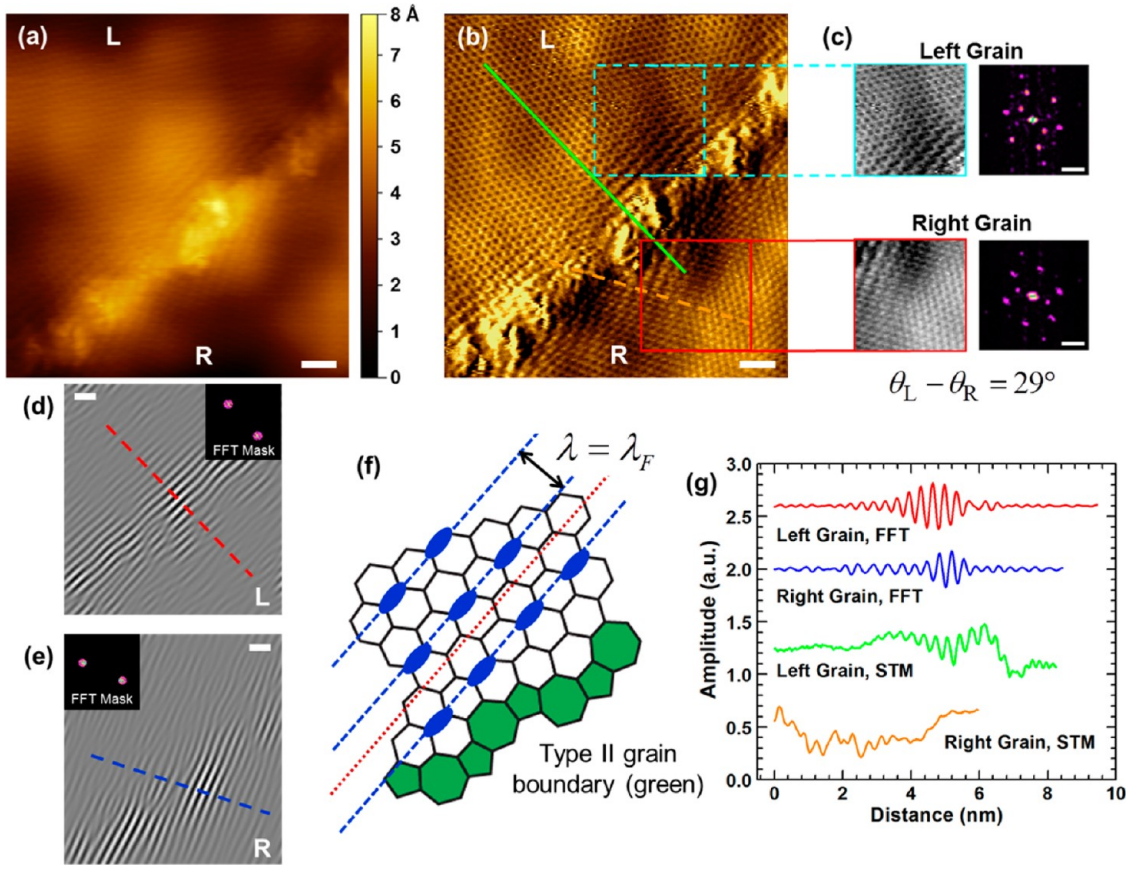

Figure 6. Linear superstructure analysis. (a) STM image of a GB between two graphene grains with a misorientation angle of ~29°, showing a linear superstructure observed on either side of the GB. (b) False-colored derivative of the STM topograph shown in (a) for better contrast. (c) Upper panel shows a section to the left (L) of the GB and the resulting 2D FFT. The six outer points forming a hexagon correspond to the reciprocal lattice of the graphene; the pair of inner points corresponds to the linear superstructure observed immediately adjacent to left of the GB. Lower panel shows a section to the right (R) of the GB and the resulting 2D FFT, similar to the upper panel. (d) FFT filtered version of the L image from (b) using the inset FFT mask, which filters out everything but the linear superstructure. (e) FFT filtered version of the R image from (b) using the inset FFT mask, which corresponds to filtering out everything but the linear superstructure. (f) Schematic model of the left side of a pentagon−heptagon GB, similar to the one shown in (a,b), but with a different misorientation angle. The blue regions illustrate the interference localization along the C−C bonds, giving a superstructure wavelength λ_F (Fermi wavelength). (g) Superstructure spatial extent, with line cuts taken perpendicular to the wavefront and offset for clarity. The two curves labeled with left and right grain FFT were extracted along the lines shown in (d) and (e), respectively. The two curves labeled with STM were extracted along the lines shown in (b). The decay length of the linear superstructure is ~1.01 nm in the left grain and ~0.49 nm in the right grain. The scale bars are all 1 nm.

Similarly, the bottom panel of Figure 6c shows a small section to the right of the GB from Figure 6b and the resulting 2D FFT. These two FFTs also have a pair of inner points that correspond to K and K′ points of the graphene Brillouin zone (BZ) on their respective GB sides.[40]

By following the 2D FFT filtering procedure in the Supporting Information and in Yang *et al.*,[41] we filtered everything but the linear superstructure patterns on the left and right sides of the GB, leaving only the linear superstructures. Figure 6d,e shows the filtering results for the linear superstructure in the left and right graphene grains, respectively, with the FFT masks that we use shown in the inset. While the propagation direction of the linear superstructure to the left of the GB in Figure 6b is close to perpendicular to the GB (~83°), the angle between the propagation direction of the linear superstructure to the right of the GB in Figure 6c and the GB is ~54°. The superstructure propagation direction in each grain is along one of the zigzag directions in that graphene grain. From the image in Figure 6b and the FFTs and filtered images in Figure 6c,d, we find that the period of this linear superstructure is ~3.7 Å. This is approximately the Fermi wavelength, $\lambda_F = 3a/2 = 3.69$ Å, where $a = 2.46$ Å is the lattice constant of graphene. Such a value was reported for linear superstructures observed adjacent to irregular armchair graphene edges on SiC.[41]

The observation of λ_F rather than $\lambda_F/2$ indicates that the interference of the scattered carriers is localized along the C−C bonds, where there are available DOS.[41] In contrast, the recent work of Tian *et al.*[42] observed a linear superstructure with period $\lambda_F/2$ adjacent to an armchair graphene edge on Cu, suggesting that the

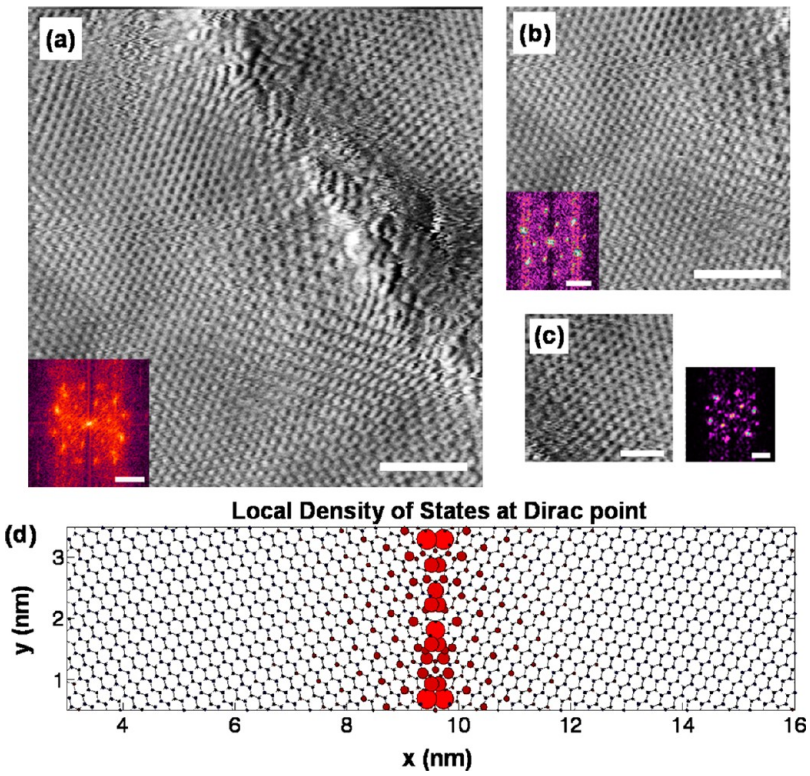

Figure 7. Intervalley scattering from a grain boundary (GB). (a) STM image of a GB between two graphene grains with a misorientation angle of ~27°, showing a $(\sqrt{3} \times \sqrt{3})R30°$ superstructure to the left of the GB. The lower left inset shows the FFT of the entire image. (b) Cropped lower left section of the STM scan (same scale) shown in (a) with just the graphene lattice and the superstructure. The inset FFT in the lower left corner shows all six points of the Brillouin zone (BZ). (c) Cropped upper right section of the STM scan from (a) shown at the same scale. The FFT of the image also shows all six points of the BZ. (d) Tight-binding simulation of a GB with 21.8° grain misorientation showing the local density of states at the Dirac point and exhibiting a $(\sqrt{3} \times \sqrt{3})R30°$ superstructure pattern. The scale bars in (a) and (b) are 2 nm. The scale bar in (c) is 1 nm. The FFT scales bar in (a), (b), and (c) are 4 nm^{-1}.

substrate electronic structure allows the interference of the scattered carriers to localize in positions off the graphene C−C bonds. The schematic shown in Figure 6f illustrates the localization of carrier interference on one side of a type II GB[14] for a GB where the two grains are misoriented by ~32°. Since the graphene grains are rotationally misoriented, the direction of the localization would be different on the other side of the GB, matching our observation for the GB in Figure 6a.

The observation of a linear superstructure adjacent to the GB shown in Figure 6a additionally suggests that each of the graphene grains has an irregular armchair edge at the point where the defects forming the GB start.[41] Furthermore, the pair of interior points in the FFT taken on either side of the GB indicates that the primary scattering mode for such GBs is backscattering.[40] Figure 6g shows line cuts taken on the left and right sides of the GB for the filtered images shown in Figure 5b,c and the topographic derivative shown in Figure 6b. Fitting the peaks of the interference patterns for the line cuts from the filtered images in Figure 6d,e (the red and blue curves) to a decaying exponential function gives decay lengths of ~1.02 ± 0.10 nm on the left side of the GB and ~0.49 ± 0.29 nm on the right side of the GB. These decay lengths are on the order of 1 nm and match the order of the average decay lengths of the enhanced empty states tunneling conductance shown in Supporting Information Figure S5 for the GB from Figure 3d−f. They are also on the same order of magnitude as the doping shifts observed at the GBs. This suggests that these decay lengths depend on the electronic structure of the GBs rather than solely thermal effects or energy spread.[41,43]

Other GBs predominantly exhibit a $(\sqrt{3} \times \sqrt{3})R30°$ superstructure on either side of the GB, as illustrated in Figure 2d,e and Figure 7 (though the pattern is more dominant along one of the zigzag directions than the other two in Figure 2d and Figure 7). In these cases, the FFTs of the STM images show a set of points corresponding to all six K and K′ points of the graphene BZ. The presence of all six points of the graphene BZ indicates that intervalley scattering is allowed between all K and K′ points.[40] Figure 7a shows an STM image of the same GB shown in Figure 2d, which has two graphene grains misoriented by ~27°, with a 2 nm scale bar. There is a clear $(\sqrt{3} \times \sqrt{3})R30°$ structure present on the left side of the GB. The inset image is the 2D FFT of the STM image. The FFT shows the expected two sets of six outer points corresponding to the

graphene reciprocal lattices on the left and right sides of the GB. There is also a set of six interior points forming a hexagon that correspond to the six K and K′ points of the BZ for the graphene grain to the left of the GB, arising from the $(\sqrt{3} \times \sqrt{3})R30°$ superstructure resolved to the left of the GB. The superstructure from the right side of the GB is faint in the FFT since there is only a small section of the right side of the GB present in the STM image compared to the left side of the GB.

The STM image shown in Figure 7b is a smaller section of the STM image shown in Figure 7a taken from the left side of the GB with the same scale. The scale bar is 2 nm. The inset 2D FFT shows the outer set of six points for the left grain graphene reciprocal lattice and all six points corresponding to the BZ. Similarly, Figure 7c shows a smaller section of the STM image from Figure 7a taken on the right side of the GB with the same scale and its corresponding 2D FFT. The scale bar for this image is 1 nm. The FFT of the graphene to the right of the GB in Figure 7c also shows a set of six out points corresponding to the reciprocal lattice of the right grain and all six interior points corresponding to the BZ. Since the FFTs on both sides of the GB show all six points of their respective BZs, this GB causes intervalley carrier scattering.[40,41] The results shown in Figure 6 and Figure 7 indicate that the local structure of the GBs affect the particular nature of the carrier scattering from the GBs.

Recent work studying mesoscopic GB transport inferred intervalley carrier scattering at the GBs from a highly localized D peak in Raman spectroscopy at the GB and from the observed intergrain weak localization.[10,21] Two recent STM studies of CVD graphene while still on the Cu growth surface[23,24] also found the $(\sqrt{3} \times \sqrt{3})R30°$ superstructures adjacent to GBs that indicate intervalley scattering from the GBs. A further STM study of graphene islands grown on Cu foil showed prominent linear superstructure from abrupt step edges (graphene−Cu) with a smaller period ($\lambda_F/2$ rather than λ_F).[42] Thus transferring the graphene to an insulating substrate is important because the conducting Cu substrate can alter the allowed carrier interference localization. This could obscure the scattering mechanisms in a technologically relevant graphene device with GBs. Our observation of intervalley scattering of carriers from the GBs is consistent with these prior studies. However, depending on the GB structure, we also find carrier backscattering from the GBs. These results indicate that the local GB topography (*e.g.*, heptagons, pentagons, and strained hexagons or any possible chemisorbed species) and grain misorientation dictate the predominant carrier scattering modes from that GB.

While our GBs showed evidence of intervalley scattering and backscattering, as seen in Figure 6 and Figure 7, we note that most of these observed GBs occurred on turbostratic bilayer graphene (see Supporting Information). Supporting Information Figure S2 shows the Moiré patterns observed in the graphene grains, highlighting the turbostratic stacking. From the extracted Moiré patterns' periods, we find that the rotational misorientation of the top and bottom layers is ∼8.5−9.5°. Theoretical and experimental studies of turbostratic graphene[44] and graphene grown on the carbon face of SiC[45,46] show that multilayer graphene behaves like stacked monolayer graphene when the layers are misoriented by more than 5°. Indeed, a study of turbostratically stacked few-layer graphene grown by CVD on polycrystalline Ni also showed that for layers misoriented by greater than ∼3° carriers still exhibited Landau level spectra indicative of massless Dirac fermions.[47] Furthermore, the plot of the local density of states (LDOS) at the Dirac point from our tight-binding simulation of a type II GB in monolayer graphene shown in Figure 7d shows a $(\sqrt{3} \times \sqrt{3})R30°$ superstructure (see Supporting Information). This confirms our observation of $(\sqrt{3} \times \sqrt{3})R30°$ superstructures adjacent to most of the graphene GBs. Thus, the observed backscattering and intervalley scattering arise from the sharp lattice defects forming the GBs and not from any turbostratic interlayer interaction.

Although we do not know the exact topological structure of the GBs in Figures 6 and 7, we can make some comparative observations about the two in an attempt to determine how the local structure affects the nature of the carrier scattering. Both GBs are formed by the merging of two graphene grains with a large misorientation angle (∼29° for Figure 6 and ∼27° for Figure 7). The electronic superstructures adjacent to each of the GBs extend approximately the same distance on either side of each GB and have approximately the same intensity. However, the scattering for the GB in Figure 6 is dominated by backscattering, and that for the GB in Figure 7 is intervalley scattering. The GB in Figure 6 seems to be a continuous line of defects, while the GB in Figure 7 has more of a semiperiodic structure with flat regions between regions that protrude more from the surface.

The small-angle GB (∼6°) in CVD graphene on mica with water trapped between the graphene and the mica[37] shown in Supporting Information Figure S8 is more periodic than the GBs given in Figures 6 and 7. The electronic superstructures adjacent to the GB in Figure S8 are also much fainter. This matches with the lack of a substantial potential barrier at this GB (see Supporting Information Figure S8c). Of the GBs shown in Figures 6, 7, S7, and S8, the GB from Figure 6 had the largest potential barrier of ∼0.1 V. The GB in Figure S8 had the smallest potential barrier of ∼0.02 V. These data suggest that the GBs which are more periodic and well-ordered like that in Supporting Information Figure S8 will have reduced carrier scattering from the GB compared to the aperiodic GBs

composed of a continuous line of defects (such as that in Figure 6).

CONCLUSIONS

In summary, we have studied GBs at the atomic scale using UHV-STM and STS for graphene grown by CVD on polycrystalline Cu foil and transferred to SiO_2. We have found that no preferred misorientation angle occurs between the as-grown graphene grains. The GBs are aperiodic, in agreement with recent TEM studies of Cu-grown graphene GBs,[17−19] and have varying heights, with an average value of 1.9 Å. As expected, the GBs strongly perturb the electronic structure of the graphene, and the GBs show an asymmetric, enhanced empty states tunneling conductance with a decay length of ∼1 nm on either side of the GB. Graphene GBs decrease the local work function, leading to *p*-*n*-*p* and *p*-*p*′-*p* (*p*′ < *p*) potential barriers that act as scatterers. Fourier analysis indicates that the GB potential barriers give both backscattering and intervalley carrier scattering, deleterious for applications involving carrier transport through polycrystalline graphene films. Combining the spectroscopic and scattering results suggest that GBs that are more periodic and well-ordered lead to reduced scattering from the GBs. Recent reported work[48] suggests that GBs may actually improve the performance of polycrystalline graphene chemical sensors. This suggests GB-selective chemistry to preferentially adsorb molecules at the GBs and mitigate the potential barrier from the GBs. Alternatively, GBs could engineer doping on the nanometer scale, enabling further studies of novel physics such as Klein tunneling[49−51] and novel devices such as a Veselago lens.[52]

METHODS

STM Measurements. A summary of our experimental methods were published in a recent report.[53] In brief, our experiments used a home-built, room-temperature ultrahigh vacuum scanning tunneling microscope (UHV-STM) with a base pressure of 3×10^{-11} Torr[54] and electrochemically etched tungsten tips. Using direct-current heating through the n^+ Si substrate, we degassed the sample in the UHV-STM system at a temperature of 600−700 °C for 24 h. In our system, the tip is grounded and the bias is applied to the sample. The current set points for the constant current topographs range from 0.1−1 nA with tip−sample biases between ±0.2 and ±1 V. We probed the local density of states (LDOS) of the sample using constant-spacing scanning tunneling spectroscopy (STS) in which the tip feedback is turned off at predetermined locations and the tip−sample bias swept through a specified range while recording the tunneling current. We measured the graphene grain misorientation angles from the rotation of the 2D FFT patterns of each graphene grain and from fitting lines to the zigzag directions of each graphene grain using the derivative of the STM topographs.

Graphene Growth and Characterization. We grew the graphene on 1.4 mil copper foil purchased from Basic Copper in an Atomate CVD system. The foils were annealed at 1000 °C under Ar/H_2 flow for 45 min, and graphene was subsequently grown under a 17:1:3 ratio of $CH_4/H_2/Ar$ flow for 30 min at an operating pressure of 2 Torr. The resulting substrates were cooled to room temperature at ∼20 °C/min under the same gas flow. After growth, the graphene was transferred onto a 90 nm SiO_2/n^+ Si substrate by first coating the graphene with a bilayer of 495K A2 and 950K A4 PMMA (MicroChem). Each PMMA layer was applied at 3000 rpm for 30 s followed by a 2 min bake at 200 °C. An O_2 RIE plasma removed the uncoated graphene on the backside of the Cu foil before etching the Cu foil in 1 M $FeCl_3$ overnight. The remaining graphene film was rinsed in deionized (DI) water to remove residual etchant before transferring to the SiO_2/Si substrate.[48] A single gold contact was shadow evaporated onto the sample to allow the STM electrical access to the graphene. After STM data were collected, we used Raman spectroscopy and atomic force microscopy (AFM) to characterize the graphene topography and quality. Raman spectroscopy was performed at 633 nm laser excitation using a Renishaw inVia Raman microscope. AFM data were collected using a Digital Instruments Veeco AFM with a Dimension IV controller.

Conflict of Interest: The authors declare no competing financial interest.

Acknowledgment. This work was supported by the Office of Naval Research through Grants N00014-06-10120 and N00014-09-0180, the Advanced Research Project Agency and Space and Naval Warfare Center under Contract N66001-08-C-2040, the National Science Foundation under Grant CHE 10-38015, the Nanoelectronics Research Initiative, the Beckman Foundation (J.W.), and the NDSEG Graduate Fellowship (D.E. and J.W.). We acknowledge helpful conversations with Prof. Nadya Mason, Dr. Bruno Uchoa, and Prof. David Ferry. We also thank Dr. Scott Schmucker for useful conversations and assistance with the STM software.

Supporting Information Available: Further discussion of the multilayer graphene, Moiré patterns, ripping the top graphene layer and their accompanying STM images are available. Analysis of the (d*I*/d*V*) spectra map in Figure 3e to obtain the decay length of the empty states enhancement at the GB and an illustration of the effect of a graphene doping shift on tunneling conductance are also available. Further STS data for GBs on mica and back-gated GBs on SiO_2/Si, and a description of the tight-binding simulation of a periodic GB are available. This material is available free of charge *via* the Internet at http://pubs.acs.org.

Note Added in Proof: During the review process, we became aware of a related computational study that further corroborates the deleterious effects of GBs on carrier transport (ref 55).

REFERENCES AND NOTES

1. Castro Neto, A. H.; Guinea, F.; Peres, N. M. R.; Novoselov, K. S.; Geim, A. K. The Electronic Properties of Graphene. *Rev. Mod. Phys.* **2009**, *81*, 109–162.
2. Berger, C.; Song, Z.; Li, T.; Li, X.; Ogbazghi, A. Y.; Feng, R.; Dai, Z.; Marchenkov, A. N.; Conrad, E. H.; First, P. N.; *et al.* Ultrathin Epitaxial Graphite: 2D Electron Gas Properties and a Route toward Graphene-Based Nanoelectronics. *J. Phys. Chem. B* **2004**, *108*, 19912–19916.
3. Unarunotai, S.; Koepke, J. C.; Tsai, C.; Du, F.; Chialvo, C. E.; Murata, Y.; Haasch, R.; Petrov, I.; Mason, N.; Shim, M.; *et al.* Layer-by-Layer Transfer of Multiple, Large Area Sheets of Graphene Grown in Multilayer Stacks on a Single SiC Wafer. *ACS Nano* **2010**, *4*, 5591–5598.
4. Reina, A.; Jia, X.; Ho, J.; Nezich, D.; Son, H.; Bulovic, V.; Dresselhaus, M. S.; Kong, J. Large Area, Few-Layer Graphene Films on Arbitrary Substrates by Chemical Vapor Deposition. *Nano Lett.* **2009**, *9*, 30–35.
5. Sutter, P. W.; Flege, J.; Sutter, E. A. Epitaxial Graphene on Ruthenium. *Nat. Mater.* **2008**, *7*, 406–411.
6. Li, X.; Cai, W.; An, J.; Kim, S.; Nah, J.; Yang, D.; Piner, R.; Velamakanni, A.; Jung, I.; Tutuc, E.; *et al.* Large-Area Synthesis of High-Quality and Uniform Graphene Films on Copper Foils. *Science* **2009**, *324*, 1312–1314.

7. Coraux, J.; N'Diaye, A. T.; Busse, C.; Michely, T. Structural Coherency of Graphene on Ir(111). *Nano Lett.* **2008**, *8*, 565–570.
8. Land, T. A.; Michely, T.; Behm, R. J.; Hemminger, J. C.; Comsa, G. STM Investigation of Single Layer Graphite Structures Produced on Pt(111) by Hydrocarbon Decomposition. *Surf. Sci.* **1992**, *264*, 261–270.
9. Wofford, J. M.; Nie, S.; McCarty, K. F.; Bartelt, N. C.; Dubon, O. D. Graphene Islands on Cu Foils: The Interplay between Shape, Orientation, and Defects. *Nano Lett.* **2010**, *10*, 4890–4896.
10. Yu, Q.; Jauregui, L. A.; Wu, W.; Colby, R.; Tian, J.; Su, Z.; Cao, H.; Liu, Z.; Pandey, D.; Wei, D.; *et al.* Control and Characterization of Individual Grains and Grain Boundaries in Graphene Grown by Chemical Vapour Deposition. *Nat. Mater.* **2011**, *10*, 443–449.
11. Li, X.; Magnuson, C. W.; Venugopal, A.; Tromp, R. M.; Hannon, J. B.; Vogel, E. M.; Colombo, L.; Ruoff, R. S. Large-Area Graphene Single Crystals Grown by Low-Pressure Chemical Vapor Deposition of Methane on Copper. *J. Am. Chem. Soc.* **2011**, *133*, 2816–2819.
12. Vlassiouk, I.; Regmi, M.; Fulvio, P.; Dai, S.; Datskos, P.; Eres, G.; Smirnov, S. Role of Hydrogen in Chemical Vapor Deposition Growth of Large Single-Crystal Graphene. *ACS Nano* **2011**, *5*, 6069–6076.
13. Wood, J. D.; Schmucker, S. W.; Lyons, A. S.; Pop, E.; Lyding, J. W. Effects of Polycrystalline Cu Substrate on Graphene Growth by Chemical Vapor Deposition. *Nano Lett.* **2011**, *11*, 4547–4554.
14. Yazyev, O. V.; Louie, S. G. Electronic Transport in Polycrystalline Graphene. *Nat. Mater.* **2010**, *9*, 806–809.
15. Yazyev, O. V.; Louie, S. G. Topological Defects in Graphene: Dislocations and Grain Boundaries. *Phys. Rev. B* **2010**, *81*, 195420.
16. Liu, Y.; Yakobson, B. I. Cones, Pringles, and Grain Boundary Landscapes in Graphene Topology. *Nano Lett.* **2010**, *10*, 2178–2183.
17. Huang, P. Y.; Ruiz-Vargas, C.; van der Zande, A. M.; Whitney, W. S.; Levendorf, M. P.; Kevek, J. W.; Garg, S.; Alden, J. S.; Hustedt, C. J.; Zhu, Y.; *et al.* Grains and Grain Boundaries in Single-Layer Graphene Atomic Patchwork Quilts. *Nature* **2011**, *469*, 389–392.
18. An, J.; Voelkl, E.; Suk, J. W.; Li, X.; Magnuson, C. W.; Fu, L.; Tiemeijer, P.; Bischoff, M.; Freitag, B.; Popova, E.; *et al.* Domain (Grain) Boundaries and Evidence of "Twinlike" Structures in Chemically Vapor Deposited Grown Graphene. *ACS Nano* **2011**, *5*, 2433–2439.
19. Kim, K.; Lee, Z.; Regan, W.; Kisielowski, C.; Crommie, M. F.; Zettl, A. Grain Boundary Mapping in Polycrystalline Graphene. *ACS Nano* **2011**, *5*, 2142–2146.
20. Nemes-Incze, P.; Yoo, K. J.; Tapasztó, L.; Dobrik, G.; Lábár, J.; Horváth, Z. E.; Hwang, C.; Biró, L. P. Revealing the Grain Structure of Graphene Grown by Chemical Vapor Deposition. *Appl. Phys. Lett.* **2011**, *99*, 023104.
21. Jauregui, L. A.; Cao, H.; Wu, W.; Yu, Q.; Chen, Y. P. Electronic Properties of Grains and Grain Boundaries in Graphene Grown by Chemical Vapor Deposition. *Solid State Commun.* **2011**, *151*, 1100–1104.
22. Gao, L.; Guest, J. R.; Guisinger, N. P. Epitaxial Graphene on Cu(111). *Nano Lett.* **2010**, *10*, 3512–3516.
23. Zhang, Y.; Gao, T.; Gao, Y.; Xie, S.; Ji, Q.; Yan, K.; Peng, H.; Liu, Z. Defect-like Structures of Graphene on Copper Foils for Strain Relief Investigated by High-Resolution Scanning Tunneling Microscopy. *ACS Nano* **2011**, *5*, 4014–4022.
24. Tapasztó, L.; Nemes-Incze, P.; Dobrik, G.; Yoo, K. J.; Hwang, C.; Biró, L. P. Mapping the Electronic Properties of Individual Graphene Grain Boundaries. *Appl. Phys. Lett.* **2012**, *100*, 053114.
25. Pan, Z.; Liu, N.; Fu, L.; Liu, Z. Wrinkle Engineering: A New Approach to Massive Graphene Nanoribbon Arrays. *J. Am. Chem. Soc.* **2011**, *133*, 17578–17581.
26. Liu, N.; Pan, Z.; Fu, L.; Zhang, C.; Dai, B.; Liu, Z. The Origin of Wrinkles on Transferred Graphene. *Nano Res.* **2011**, *4*, 996–1004.
27. Ferrari, A. C.; Meyer, J. C.; Scardaci, V.; Casiraghi, C.; Lazzeri, M.; Mauri, F.; Piscanec, S.; Jiang, D.; Novoselov, K. S.; Roth, S.; *et al.* Raman Spectrum of Graphene and Graphene Layers. *Phys. Rev. Lett.* **2006**, *97*, 187401.
28. Ruiz-Vargas, C.; Zhuang, H. L.; Huang, P. Y.; van der Zande, A. M.; Garg, S.; McEuen, P. L.; Muller, D. A.; Hennig, R. G.; Park, J. Softened Elastic Response and Unzipping in Chemical Vapor Deposition Graphene Membranes. *Nano Lett.* **2011**, *11*, 2259–2263.
29. Červenka, J.; Flipse, C. F. J. Structural and Electronic Properties of Grain Boundaries in Graphite: Planes of Periodically Distributed Point Defects. *Phys. Rev. B* **2009**, *79*, 195429.
30. Červenka, J.; Katsnelson, M. I.; Flipse, C. F. J. Room-Temperature Ferromagnetism in Graphite Driven by Two-Dimensional Networks of Point Defects. *Nat. Phys.* **2009**, *5*, 840–844.
31. Feenstra, R. M.; Stroscio, J. A.; Fein, A. P. Tunneling Spectroscopy of the Si(111)2 $\times$ 1 Surface. *Surf. Sci.* **1987**, *181*, 295–306.
32. Hamers, R. J.; Padowitz, D. F. Methods of Tunneling Spectroscopy with the STM. In *Scanning Probe Microscopy and Spectroscopy: Theory, Techniques, and Applications*; Bonnell, D. A., Ed.; Wiley-VCH: New York, 2001; pp 59–110.
33. Levy, N.; Burke, S. A.; Meaker, K. L.; Panlasigui, M.; Zettl, A.; Guinea, F.; Neto, A. H. C.; Crommie, M. F. Strain-Induced Pseudo-Magnetic Fields Greater than 300 T in Graphene Nanobubbles. *Science* **2010**, *329*, 544–547.
34. Deshpande, A.; Bao, W.; Miao, F.; Lau, C. N.; LeRoy, B. J. Spatially Resolved Spectroscopy of Monolayer Graphene on SiO_2. *Phys. Rev. B* **2009**, *79*, 205411.
35. Zhao, L.; He, R.; Rim, K. T.; Schiros, T.; Kim, K. S.; Zhou, H.; Gutiérrez, C.; Chockalingam, S. P.; Arguello, C. J.; Pálová, L.; *et al.* Visualizing Individual Nitrogen Dopants in Monolayer Graphene. *Science* **2011**, *333*, 999–1003.
36. Lv, R.; Li, Q.; Botello-Méndez, A. R.; Hayashi, T.; Wang, B.; Berkdemir, A.; Hao, Q.; Elías, A. L.; Cruz-Silva, R.; Gutiérrez, H. R.; *et al.* Nitrogen-Doped Graphene: Beyond Single Substitution and Enhanced Molecular Sensing. *Sci. Rep.* **2012**, *2*, 586.
37. He, K. T.; Wood, J. D.; Doidge, G. P.; Pop, E.; Lyding, J. W. Scanning Tunneling Microscopy Study and Nanomanipulation of Graphene-Coated Water on Mica. *Nano Lett.* **2012**, *12*, 2665–2672.
38. Zhang, Y.; Brar, V. W.; Girit, C.; Zettl, A.; Crommie, M. F. Origin of Spatial Charge Inhomogeneity in Graphene. *Nat. Phys.* **2009**, *5*, 722–726.
39. Xue, J.; Sanchez-Yamagishi, J.; Bulmash, D.; Jacquod, P.; Deshpande, A.; Watanabe, K.; Taniguchi, T.; Jarillo-Herrero, P.; LeRoy, B. J. Scanning Tunnelling Microscopy and Spectroscopy of Ultra-flat Graphene on Hexagonal Boron Nitride. *Nat. Mater.* **2011**, *10*, 282–285.
40. Rutter, G. M.; Crain, J. N.; Guisinger, N. P.; Li, T.; First, P. N.; Stroscio, J. A. Scattering and Interference in Epitaxial Graphene. *Science* **2007**, *317*, 219–222.
41. Yang, H.; Mayne, A. J.; Boucherit, M.; Comtet, G.; Dujardin, G.; Kuk, Y. Quantum Interference Channeling at Graphene Edges. *Nano Lett.* **2010**, *10*, 943–947.
42. Tian, J.; Cao, H.; Wu, W.; Yu, Q.; Chen, Y. P. Direct Imaging of Graphene Edges: Atomic Structure and Electronic Scattering. *Nano Lett.* **2011**, *11*, 3663–3668.
43. Hasegawa, Y.; Avouris, P. Direct Observation of Standing Wave Formation at Surface Steps Using Scanning Tunneling Spectroscopy. *Phys. Rev. Lett.* **1993**, *71*, 1071–1074.
44. Shallcross, S.; Sharma, S.; Kandelaki, E.; Pankratov, O. A. Electronic Structure of Turbostratic Graphene. *Phys. Rev. B* **2010**, *81*, 165105.
45. Hass, J.; Varchon, F.; Millán-Otoya, J. E.; Sprinkle, M.; Sharma, N.; de Heer, W. A.; Berger, C.; First, P. N.; Magaud, L.; Conrad, E. H. Why Multilayer Graphene on 4H-SiC($000\bar{1}$) Behaves Like a Single Sheet of Graphene. *Phys. Rev. Lett.* **2008**, *100*, 125504.
46. Sprinkle, M.; Hicks, J.; Taleb-Ibrahimi, A.; Le Fèvre, P.; Bertran, F.; Tinkey, H.; Clark, M. C.; Soukiassian, P.; Martinotti, D.; Hass, J.; *et al.* Multilayer Epitaxial Graphene

Grown on the SiC Surface; Structure and Electronic Properties. *J. Phys. D: Appl. Phys.* **2010**, *43*, 374006.
47. Luican, A.; Li, G.; Reina, A.; Kong, J.; Nair, R. R.; Novoselov, K. S.; Geim, A. K.; Andrei, E. Y. Single-Layer Behavior and Its Breakdown in Twisted Graphene Layers. *Phys. Rev. Lett.* **2011**, *106*, 126802.
48. Salehi-Khojin, A.; Estrada, D.; Lin, K. Y.; Bae, M.; Xiong, F.; Pop, E.; Masel, R. I. Polycrystalline Graphene Ribbons as Chemiresistors. *Adv. Mater.* **2012**, *24*, 53–57.
49. Stander, N.; Huard, B.; Goldhaber-Gordon, D. Evidence for Klein Tunneling in Graphene p-n Junctions. *Phys. Rev. Lett.* **2009**, *102*, 026807.
50. Young, A. F.; Kim, P. Quantum Interference and Klein Tunnelling in Graphene Heterojunctions. *Nat. Phys.* **2009**, *5*, 222–226.
51. Katsnelson, M. I.; Novoselov, K. S.; Geim, A. K. Chiral Tunnelling and the Klein Paradox in Graphene. *Nat. Phys.* **2006**, *2*, 620–625.
52. Cheianov, V. V.; Fal'ko, V.; Altshuler, B. L. The Focusing of Electron Flow and a Veselago Lens in Graphene p-n Junctions. *Science* **2007**, *315*, 1252–1255.
53. Koepke, J. C.; Wood, J. D.; Estrada, D.; Ong, Z.-Y.; Xiong, F.; Pop, E.; Lyding, J. W. Atomic-Scale Study of Scattering and Electronic Properties of CVD Graphene Grain Boundaries. *Proceedings of the IEEE Conference on Nanotechnology 2012*, Birmingham, UK, 20−23 Aug. **2012**, pp. 1−4. DOI: 10.1109/NANO.2012.6322107.
54. Brockenbrough, R. T.; Lyding, J. W. Inertial Tip Translator for a Scanning Tunneling Microscope. *Rev. Sci. Instrum.* **1993**, *64*, 2225–2228.
55. Ferry, D. K. Short-Range Potential Scattering and Its Effect on Graphene Mobility. Submitted for publication.

Supporting Information

Atomic-Scale Evidence for Potential Barriers and Strong Carrier Scattering at Graphene Grain Boundaries: a Scanning Tunneling Microscopy Study

Justin C. Koepke[1,2*], Joshua D. Wood[1,2,3], David Estrada[1,3], Zhun-Yong Ong[3,4], Kevin He[1,2], Eric Pop[1,2,3], Joseph W. Lyding[1,2,3*]

[1]*Dept. of Electrical & Computer Eng., University of Illinois, Urbana-Champaign, IL 61801, USA*

[2]*Beckman Institute for Advanced Science and Technology, University of Illinois, Urbana-Champaign, IL 61801, USA*

[3]*Micro & Nanotechnology Lab, University of Illinois, Urbana-Champaign, IL 61801, USA*

[4] *Dept. of Physics, University of Illinois, Urbana-Champaign, IL 61801, USA*

*Contacts: jkoepke@illinois.edu, lyding@illinois.edu

Contents:

- **I. Turbostratic Graphene**
- **II. Ripped Graphene Section**
- **III. Decay Length of Enhanced Empty States Tunneling Conductance**
- **IV. Spectroscopy of Graphene Grain Boundaries on Mica**
- **V. Spectroscopy of Back-Gated Graphene Grain Boundaries on SiO_2/Si**
- **VI. Tight-binding Grain Boundary Simulation**
- **References**
- **Figure S1. Moiré patterns**
- **Figure S2. Moiré pattern adjacent to grain boundary.**
- **Figure S3. Ripped graphene section.**
- **Figure S4. Voltage cuts of dI/dV spectra map.**
- **Figure S5. Decay length of enhanced empty states tunneling conductance at grain boundary.**
- **Figure S6. Illustration of effect of graphene doping shift on tunneling conductance**
- **Figure S7. Large angle graphene grain boundary (GB) spectroscopy on mica.**
- **Figure S8. Small angle graphene grain boundary (GB) spectroscopy on mica.**
- **Figure S9. Small angle graphene grain boundary (GB) on and off GB tunneling conductance comparison.**
- **Figure S10. Tunneling spectroscopy of back-gated CVD graphene grain boundary (GB): V_{BG} = -10V.**
- **Figure S11. Tunneling spectroscopy of back-gated CVD graphene grain boundary (GB): V_{BG} = -15V.**
- **Figure S12. Tight binding simulation of a grain boundary.**

I. Turbostratic Graphene

The parameters used during the graphene growth process differed from those reported in the original paper describing CVD of graphene on Cu foil.[1] The methane flux was higher in our growth process. The contrast differences in the optical microscopy as shown in Figure 1a suggest that this growth process created regions of monolayer graphene and regions of bilayer graphene, as confirmed through Raman spectroscopy measurements of the G'/G (2D/G) peak intensity ratio, commonly used to characterize mechanically-exfoliated graphene as monolayer or multiple layers.[2] However, we note that a better Raman metric for determining whether the graphene is monolayer or bilayer is to use the shear mode recently reported by Tan *et al.*.[3] The values of G'/G (2D/G) peak intensity ratios for this sample suggest that at least some of the regions are bilayer graphene.

Scanning tunneling microscopy (STM) scans of the sample confirmed that the growth process yielded regions of bilayer graphene. Figure S1a shows the derivative of a 71.5 nm × 76.5 nm STM topographic image of a GB between two graphene grains misoriented by ~29°. There are definite Moiré patterns on each side of the GB. The presence of the Moiré patterns indicates that two layers of turbostratically-stacked graphene[4] are present on either side of the GB. The periodicity of the pattern suggests that the two layers to the right of the GB are rotated by ~13°. The two-dimensional fast Fourier transforms (2D-FFTs) of the lower-left and upper-right regions from Figure S1a, shown in Figures S1b and S1c, respectively, indicate that two different Moiré patterns are present on either side of the GB rotated with respect to one another by ~29°. The scale bars are 1 nm^{-1} for both Figures S1b and S1c. The FFT of the region on the right side of the GB (Figure S1b) indicates that the Moiré pattern on the right side of the GB has a larger period than that indicated by the FFT of the region on the left side of the GB (Figure S1c). The expression for the periodicity, *D*, of the Moiré pattern formed by two graphene lattices, with lattice constant d = 0.246 nm, rotated with respect to one another by an angle θ is[5]

$$D = d/\left[2\sin\left(\theta/2\right)\right].$$

Using this equation, we extract the layer misorientation of each side of the grain boundary. The misorientation of two layers of graphene on the left side of the GB is ~27°; while the misorientation of the two layers of graphene on the right side of the GB is ~13°.

Figure S2 illustrates the extraction of the Moiré period from the STM image. The GB on the left side of Figure S2a circled in green is the same one depicted in Figure 2a and Figure 6 from the main manuscript. The derivative of this STM topograph shown in Figure S2b offers better contrast and exhibits a clearly visible Moiré pattern to the right of the GB. Figure S2c, taken from the small section from within the red box in Figure S2b, shows this pattern more clearly. The 2D-FFT of this small section displayed in Figure S2d shows sets of points corresponding to the Moiré pattern. The spots are relatively weak due to the small sample size (128 x 128 pixels) and the faintness of the Moiré pattern in the image. Figure S2e shows the filter mask applied to the image from Figure S2c. The resulting filtered version of the image from Figure S2c shown in Figure S2f gives a period of ~1.5–1.65 nm. Using the above equation for the periodicity of the Moiré pattern, this implies that the top graphene layer and the bottom graphene layer are misoriented by ~8.5–9.5°.

II. Ripped Graphene Section

Prior studies of graphite using atmospheric-pressure STM have demonstrated the ability to pattern the top layer of graphite using an STM tip in air[6] or in a controlled environment with oxygen or oxygen-containing molecules.[7] A recent paper[8] suggests that rips induced by an AFM cantilever originate at GBs. We were able to rip out a section of graphene using the STM tip under UHV conditions. Figure S3a shows an STM topograph of an area with two GBs forming a right angle. Figure S3b shows the derivative of the topograph from Figure S3a for additional contrast. The image shows a Moiré pattern in the lower-left corner of the scan. After a strong STM tip-surface interaction, we observed a rip in the top layer of graphene, as shown in the STM topograph in Figure S3c and the derivative of the topograph shown in Figure S3d. The termination of the left end of the rip at the grain boundary suggests that the rip may have nucleated at the GB. That the tip can image in the ripped region also indicates (in addition to the Moiré pattern) that this was a region of bilayer graphene. Figure S3e shows a subsequent STM topograph of the area with the ripped section. The derivative of the topograph from Figure S3e shown in Figure S3f indicates the misorientation of the left grain of the top layer with the right grain of the top layer and the bottom layer of graphene. The red, green, and blue lines indicate one of the zigzag directions in the left grain of the top graphene layer, the bottom graphene layer, and the right grain of the top layer, respectively. From the resolution of Figure S3f, we can identify the misorientation between the left grain and the right grain of the top layer as ~27°. The right grain of the top graphene layer and the bottom graphene layer are rotationally misoriented by ~19°; and the left grain of the top graphene layer and the bottom graphene layer are rotationally misoriented by ~8–8.5°. Using equation (1) from above, the obtained Moiré period is ~1.66 nm, which matches the spacing of the observed Moiré pattern to the left of the GB. Thus, the GB is only in the top layer of the graphene.

III. Decay Length of Enhanced Empty States Tunneling Conductance

The constant-voltage cuts of the tunneling conductance (dI/dV) spectra map across the GB from Figure 3(e) shown in Figure S4 illustrate the enhancement of the (dI/dV) in empty states at the GB. The x-axis scale is the same for the three plots, but the y-axis scales are different. The dashed, vertical green line on the plots indicates the location of the GB. The individual cuts at V = +0.1012 V, V = +0.2114 V, and V = +0.4218 V each show larger (dI/dV) at the GB relative to the (dI/dV) for the areas away from the GB. The absolute tunneling conductance is smaller for the smaller tip-sample biases, as expected. However, the enhancement at the GB is still present. We extracted the decay lengths plotted in the subsequent figure (Figure S4) using constant tip-sample bias cuts of the (dI/dV) spectra map from Figure 3(e) in the main manuscript. These are calculated on both the left and the right sides of the GB for each empty states tip-sample bias cut.

Figure S5 shows the extracted decay length of the enhanced empty states (dI/dV) from the data shown in Figure 3e of the main manuscript plotted as a function of tip-sample bias. The blue, open triangles represent the decay lengths extracted to the right side of the GB, and the red, open circles represent the decay lengths extracted to the left side of the GB. These values were

extracted by fitting an exponential decay to the left or right side of the GB to each voltage cut from the spectra map in Figure 3e of the main manuscript. The average decay length on the left side of the GB is 0.90±0.29 nm, and that to the right side of the GB is 1.18±0.39 nm. The decay lengths of ~1 nm on average indicate that the perturbation to the electronic structure caused by the presence of the GB decays on the order of 1 nm away from the GB.

IV. Spectroscopy of Graphene Grain Boundaries on Mica

We examine UHV scanning tunneling spectroscopy (STS) of CVD graphene transferred onto a freshly cleaved mica surface[9] to compare the effect of a different substrate on the graphene GB spectroscopy. The details of the sample preparation can be found in a recent report,[9] which also examined the water trapped between the mica and the graphene. Recent Raman spectroscopy measurements of exfoliated graphene on mica found that the doping, as determined by Raman spectroscopy, was lower than expected for graphene on bare mica. The lowered doping resulted from water trapped between graphene and the mica, which effectively screens the p-type mica. Our spectroscopic results for CVD graphene transferred to mica with trapped water layers underneath also finds low doping.[9] The first GB described here occurs in a region of bilayer graphene, while the second GB is in a region of monolayer graphene.

Figure S7 shows STS data collected for a large angle GB in a region of bilayer CVD graphene on mica with water trapped between the graphene and mica. The STM topograph in Figure S7a shows a grain boundary with a grain misorientation angle of ~29° and a 2 nm scale bar. The red, horizontal line shows the location of a line of STS points across the GB. For this GB, we obtain the tunneling conductance (*dI/dV*) by differentiating the *I – V* spectra. The spectra map in Figure S5b plots the (*dI/dV*) *versus* tip-sample bias and position along the line indicated in Figure S7a with a color scale to the far right. The spectra map shows locally enhanced empty states (*dI/dV*) at the GB. The horizontal cut at a constant tip-sample bias of +0.21 V (along the horizontal, blue line) shown above the spectra map illustrates this local empty states (*dI/dV*) enhancement. Individual (*dI/dV*) curves taken on and off the GB plotted to the right of the spectra map also show the enhanced empty states (*dI/dV*) at the GB. These curves also show a shift in the tip-sample bias of the minimum of the curve for the "On GB" curve.

Figure S7c gives a plot of the tip-sample bias of the minimum of the each (*dI/dV*) curve *versus* position along the line from Figure S7a. There is an apparent decrease in the tip-sample bias of the (*dI/dV*) minimum approaching the GB. The red curve is a Gaussian fit of the data, which gives an extracted shift of ~ -0.060 V and a bulk value of +0.024 V. Since there are no secondary minima in the (*dI/dV*) and the doping of graphene on water on mica is known to be very low,[9,10] the minimum of the (*dI/dV*) should correspond to the Dirac point.[11] This leads to a p-type doping in the bulk of $\sim 4.2\times10^{10}$ cm^{-2}. The presence of the ~60 mV barrier at the GB inverts the carrier concentration to n-type doping of $\sim 9.5\times10^{10}$ cm^{-2}.

Figure S8 shows STS data collected for a small angle GB in a region of monolayer CVD graphene on mica also with water trapped between the graphene and the mica. The misorientation angle between the two graphene grains shown in the STM topograph in Figure S8a is ~6°. The scale bar is 2 nm, and the red, horizontal line indicates the location of a line of

STS points across the GB. We used standard lock-in techniques to acquire the (*dI/dV*) spectra for this GB. As with the prior figure, Figure S8b shows a spectra of the (*dI/dV*) *versus* tip-sample bias and position along the line indicated in Figure S8a. The spectra map shows definite local enhancement of empty states (*dI/dV*) and very slight enhancement of filled states (*dI/dV*) at the GB. The plot above the spectra map shows a constant tip-sample bias cut of the spectra map at +0.35 V, as indicated by the horizontal, blue line on the spectra map. This illustrates the locally enhanced empty states (*dI/dV*) at the GB (near position ~11 nm). The plot to the right of the spectra map shows vertical cuts of the spectra map at the positions indicated to the "Left of GB" and "On GB." These (*dI/dV*) spectra further illustrate the locally enhanced (*dI/dV*) at the GB and show a small shift in the minimum of the (*dI/dV*) on the GB compared to the left of the GB.

Figure S8c shows a plot of the minimum of the (*dI/dV*) spectra *versus* position along the line from Figure S8a. Unlike the large angle GB from Figure S7, the apparent shift in the minimum of the (*dI/dV*) due to this small angle GB is small. The attempted Gaussian fit shown in the red line suggests a shift in the position of only – 0.026V. This shift is the room-temperature thermal voltage. Since this fit is obviously very poor, it is on the figure merely to serve as a guide to the eye. Figure S9 shows a comparison of the average (*dI/dV*) of 13 spectra points each to the left and the right of the GB and 11 spectra points on the GB, equivalent to averaging over 1.2 nm and 1 nm, respectively. The full comparison of the three averages shown in Figure S9a illustrates the enhanced empty states (*dI/dV*) on the GB compared to the surrounding graphene, just as observed for CVD graphene GBs on SiO_2/Si described in the main manuscript. Figure S9b shows a magnified section of plot for small tip-sample biases with the bias value of the (*dI/dV*) minimum for each average. While the tip-sample bias of the (*dI/dV*) minimum decreases by ~ 0.020 V on the GB from the region to the left of the GB, it also decreases by ~0.020 V to the right of the GB. Hence whatever potential barrier this GB induces, it is insignificant compared to the local doping fluctuations and the thermal energy. The difference in background doping fluctuations between Figure S7c and Figure S8c suggests that there is more local doping fluctuation for the graphene directly in contact with the water on mica than for graphene sitting on another graphene layer in contact with the water on mica.

Comparing the results of Figures S7, S8, and S9 suggests that the height of the potential barrier that the GB induces depends on the particular GB in question (*i.e.*, the misorientation angle of the two graphene grains and the nature of the defects comprising the GB). This would seem to corroborate the theoretical predictions of different transport barriers for different graphene GB types.[12] Furthermore, the difference in background doping fluctuation between the bilayer graphene region from Figure S7 and the monolayer region from Figure S8 shows that the background doping fluctuations may swamp the effect of GBs with small potential barriers.

V. Spectroscopy of Back-Gated Graphene Grain Boundaries on SiO_2/Si

In order to study the effect of a back-gate on the doping shift due to the GBs, we transfer CVD graphene to 300 nm SiO_2/n^+ Si in the manner described in the Methods section and mount the sample to isolate the graphene from the n^+ Si, which we use to back-gate the graphene. However, due to our sample mounting arrangement, we could not degas the sample in the same way as described in the Methods section. While the degas time was still greater than 24 hours,

we were only able to heat the sample to ~ 130 °C in the UHV system. Prior to sample mounting and loading into the UHV system, we annealed the sample under turbo vacuum (~10^{-5} Torr) at 600 K for ~ 12 hours to help remove PMMA residues from the transfer process. Such vacuum annealing followed by exposure to ambient air (as in this case) strongly p-dopes the graphene due to adsorption of H_2O and O_2 molecules.[13] So unlike the non-back-gated CVD graphene on SiO_2/Si sample described in the main manuscript, we expect this sample to be heavily p-doped.[14] We employ standard lock-in techniques to acquire the (*dI/dV*) spectra for the back-gated graphene GBs.

Figure S10a shows an STM image of a CVD graphene GB with a grain misorientation angle of ~12°. Despite the imperfect resolution, there is evidence of superstructures immediately adjacent to the GB, indicating scattering. The back-gate bias (V_{BG}) for the spectra in this figure is −10 V. Figure S10b shows a (*dI/dV*) spectra map as a function of tip-sample bias and position along the green line in Figure S10a. There is an apparent state near the 5 nm position corresponding to the location of the GB. The spectra map shows minima near 0 V and also apparent secondary minima at positive tip-sample bias. These are not present in the STS data for the graphene sample in the main manuscript, which was degassed at high temperatures in UHV. The plot above the spectra map shows a constant tip-sample bias cut of the spectra map at +0.51 V, as indicated by the horizontal, gray line on the spectra map. This cut shows locally higher (*dI/dV*) at the GB than in the surrounding graphene. The plot to the right of the spectra map shows a comparison of (*dI/dV*) spectra from the left of the GB, right of the GB, and on the GB as indicated by the vertical lines on the spectra map. These (*dI/dV*) spectra show secondary minima near +0.5 V to the left and right of the GB and a secondary minimum near +0.7 V on the GB.

Figure S10c shows a plot of the secondary (not near zero) minimum of the *(dI/dV)* spectra *versus* position along the line from Figure S10a. In contrast to the data in Figure 5 of the main manuscript (high-temperature degassed CVD graphene on SiO_2/Si) and Figures S7 and S8 (high-temperature degassed CVD graphene on mica), the shift in the tip-sample bias of the secondary minimum at the GB for the back-gated sample is to larger, positive tip-sample bias. The red curve indicates a Gaussian fit for the data. The fit gives a background value of the tip-sample bias of the secondary (*dI/dV*) minimum of ~ +0.487 V and a shift of +0.239 V at the GB. These values correspond to 1.7×10^{13} cm^{-2} p-type doping away from the GB and 3.9×10^{13} cm^{-2} p-type doping at the GB. The value of 1.7×10^{13} cm^{-2} p-type doping away from the GB matches well with the value found by Raman spectroscopy for vacuum annealed graphene on SiO_2/Si subsequently exposed to air.[13]

This shift towards higher p-type carrier concentration at the GB conflicts with the observed shift towards lower p-type carrier concentration or to n-type carrier concentration at the GB for CVD graphene on SiO_2/Si degassed at higher temperatures in UHV (600-700 °C) described in the main manuscript. It also conflicts with the observations for CVD graphene on mica which has water trapped between the graphene and mica (degassed 650-700 °C in UHV). For those systems (Figures 3, 4, 5, S7, and S8), the presence of the GB decreases the local work function (or shifts the doping more towards n-type). After the vacuum anneal and subsequent ambient air exposure of the back-gated sample, we expect heavy p-type doping from adsorption of H_2O and O_2 molecules.[13] Density-functional tight-binding simulations of GBs predict that they are more chemically reactive than pristine graphene,[15] and recent sensor experiments with

CVD graphene ribbons also suggest that the GBs are more reactive.[16] Thus, the heavier p-type doping of the GBs likely arises from higher adsorption of H_2O and O_2 molecules at the GBs due to their increased reactivity. Based upon the ability to recover the low-doped state with proper heating of the sample in vacuum after ambient exposure,[13] we expect that the GBs for back-gated samples would also follow the trend in decreased work function compared to the bulk graphene grains.

We perform the same spectral analysis on the same GB in Figure S10 for $V_{BG} = -15$ V in Figure S11. Figure S11a shows the same GB as Figure S10a with a 12° misorientation angle between the two graphene grains. The green line indicates the location of the spectra points recorded with $V_{BG} = -15$ V. Figure S11b shows a map of the (*dI/dV*) spectra *versus* tip-sample bias and position along the line. Again, there are apparent minima near 0 V and secondary minima in empty states. The plot above the spectra map, again, shows a constant tip-sample bias cut (at +0.51 V) of the spectra map. The local enhancement of the empty states (*dI/dV*) at the GB is less pronounced than in Figure S10b. The plot to the right of the spectra map shows a comparison of (*dI/dV*) spectra to the left of the GB, to the right of the GB, and on the GB, as indicated by the vertical lines on the spectra map. Again, the shift to larger tip-sample bias of the secondary minimum on the GB than to the left or the right of the GB is apparent.

Figure S11c similarly shows a plot of the secondary (not near zero) minimum of the *(dI/dV)* spectra *versus* position along the line from Figure S11a. As with the data in Figure S10, the shift in the tip-sample bias of the secondary minimum of the *(dI/dV)* at the GB is towards larger tip-sample biases. However, the value of the shift is smaller than for the $V_{BG} = -10$ V case in Figure S10. From the Gaussian fit shown by the red curve, the bulk value of the tip-sample bias of the secondary *(dI/dV)* minimum is +0.507 V; the barrier at the GB is +0.155 V. These values correspond to p-type doping of 1.9×10^{13} cm^{-2} in the bulk and 3.2×10^{13} cm^{-2} at the GB. While the increase in the bulk value for the larger, $V_{BG} = -15$ V, back-gate bias is expected, the decrease in the apparent barrier at the GB and decrease in doping level are not. We are not certain of the origin of this phenomenon, but further exploration of the effect of the back-gate on the doping of the GBs relative to that of the bulk graphene is in progress. Determining whether the GB doping level scales in the same way as bulk graphene, with the square root of the back-gate bias,[17] or in a different fashion will be important for understanding transport through graphene GBs.

VI. Tight-binding Grain Boundary Simulation

To generate the lattice structure with the GB in Figures S12a and S12b, we follow the prescription given by Yazyev and Louie.[18] Each GB consists of a one-dimensional chain of closely packed (1,0) dislocations parallel to the y-axis. The boundaries are spaced ~9.6 nm apart in the x-direction. Periodic boundary conditions are imposed in the x and y-directions to avoid any spurious edge effects. The GBs partition the 3808-atom lattice into two subdomains with a misorientation angle of 21.8° between the subdomains.

To simulate the local density of state (LDOS), we use a simple nearest-neighbor tight-binding model for the π electron network. The tight-binding model Hamiltonian is

$$H = -t\sum_{i,j}\left(a_i^{\dagger}a_j + h.c.\right),$$

where t (=3.0 eV) is the transfer integral between nearest-neighbor sites, $a_i^{\dagger}$ (a_i) is the creation (annihilation) operator, i is the index of the i-th lattice site, and *h.c.* is the Hermitian conjugate. As there are 3808 sites in the lattice, the Hamiltonian can be represented with [H], a 3808 by 3808 matrix, with the non-zero matrix elements equal to the transfer integral. By diagonalizing [H], we are able to obtain the eigenenergies ε_n and their corresponding eigenfunctions ψ_n in the form of a 3808-element vector. Each component of the eigenvector represents the overlap between the eigenfunction and the lattice site. Therefore, the squared local amplitude of the eigenfunction corresponds to the LDOS at that site.

Assuming that the system is charge neutral, the LDOS is determined by the local squared amplitude of the eigenstates around $\varepsilon_n = 0$ *in excess* of the background squared amplitude, because the states with $\varepsilon_n < 0$ are filled and the electron can only tunnel to the empty states. Therefore, to plot the LDOS on site i, we compute the excess local squared amplitude of the $\varepsilon_n = 0$ eigenstates

$$\rho_i = \frac{1}{4}\sum_n \left|\langle i|\psi_n\rangle\right|^2 - \frac{1}{\sum_i \left|\langle i|i\rangle\right|^2},$$

where the sum is over 4 eigenstates around $\varepsilon_n = 0$. The first term on the right hand side represents the empty LDOS and the second term the filled background LDOS. For ease of visualization, we set the size of the (red) circles to be proportional to ρ_i in Figure S12a.

The plot in Figure S12a clearly shows a $\left(\sqrt{3}\times\sqrt{3}\right)R30°$ superstructure adjacent to the GB. This superstructure is the same as that observed adjacent to the GBs in the STM images, depending on the tip resolution and the tunneling conditions. It also displays the localized states at the boundary. The plot in Figure S12a is also shown in Figure 7d in the main text. Figure S12b shows the physical lattice structure used in the tight-binding calculation.

References

(1) Li, X.; Cai, W.; An, J.; Kim, S.; Nah, J.; Yang, D.; Piner, R.; Velamakanni, A.; Jung, I.; Tutuc, E.; *et al*. Large-Area Synthesis of High-Quality and Uniform Graphene Films on Copper Foils. *Science* **2009**, *324*, 1312-1314.

(2) Ferrari, A. C.; Meyer, J. C.; Scardaci, V.; Casiraghi, C.; Lazzeri, M.; Mauri, F.; Piscanec, S.; Jiang, D.; Novoselov, K. S.; Roth, S.; *et al*. Raman Spectrum of Graphene and Graphene Layers. *Phys. Rev. Lett.* **2006**, *97*, 187401.

(3) Tan, P. H.; Han, W. P.; Zhao, W. J.; Wu, Z. H.; Chang, K.; Wang, H.; Wang, Y. F.; Bonini, N.; Marzari, N.; Pugno, N.; *et al*. The Shear Mode of Multilayer Graphene. *Nat. Mater.* **2012**, *11*, 294-300.

(4) Biedermann, L. B.; Bolen, M. L.; Capano, M. A.; Zemlyanov, D.; Reifenberger, R. G. Insights into Few-Layer Epitaxial Graphene Growth on 4H-SiC ($000\bar{1}$) Substrates from STM Studies. *Phys. Rev. B* **2009**, *79*, 125411.

(5) Pong, W.; Durkan, C. A Review and Outlook for an Anomaly of Scanning Tunnelling Microscopy (STM): Superlattices on Graphite. *J. Phys. D: Appl. Phys.* **2005**, *38*, R329.

(6) Mizutani, W.; Inukai, J.; Ono, M. Making a Monolayer Hole in a Graphite Surface by Means of a Scanning Tunneling Microscope. *Jpn. J. Appl. Phys.* **1990**, *29*, L815-L817.

(7) Park, J.; Kim, K. B.; Park, J.; Choi, T.; Seo, Y. Graphite Patterning in a Controlled Gas Environment. *Nanotechnology* **2011**, *22*, 335304.

(8) Ruiz-Vargas, C.; Zhuang, H. L.; Huang, P. Y.; van der Zande, A. M.; Garg, S.; McEuen, P. L.; Muller, D. A.; Hennig, R. G.; Park, J. Softened Elastic Response and Unzipping in Chemical Vapor Deposition Graphene Membranes. *Nano Lett.* **2011**, *11*, 2259-2263.

(9) He, K. T.; Wood, J. D.; Doidge, G. P.; Pop, E.; Lyding, J. W. Scanning Tunneling Microscopy Study and Nanomanipulation of Graphene-Coated Water on Mica. *Nano Lett.* **2012**, *12*, 2665-2672.

(10) Shim, J.; Lui, C. H.; Ko, T. Y.; Yu, Y. -J.; Kim, P.; Heinz, T. F; Ryu, S. Water-Gated Charge Doping of Graphene Induced by Mica Substrates. *Nano Lett.* **2012**, *12*, 648-654.

(11) Deshpande, A.; Bao, W.; Miao, F.; Lau, C. N.; LeRoy, B. J. Spatially Resolved Spectroscopy of Monolayer Graphene on SiO_2. *Phys. Rev. B* **2009**, *79*, 205411.

(12) Yazyev, O. V.; Louie, S. G. Electronic Transport in Polycrystalline Graphene. *Nat. Mater.* **2010**, *9*, 806-809.

(13) Ni, Z. H.; Wang, H. M; Luo, Z. Q.; Wang, Y. Y.; Yu, T.; Wu, Y. H.; Shen, Z. X. The Effect of Vacuum Annealing on Graphene. *J. Raman Spectrosc.* **2010**, *41*, 479-483.

(14) Lin, Y.; Lu, C.; Yeh, C.; Jin, C.; Suenaga, K.; Chiu, P. Graphene Annealing: How Clean Can It Be? *Nano Lett.* **2012**, *12*, 414-419.

(15) Malola, S.; Häkkinen, H.; Koskinen, P. Structural, Chemical, and Dynamical Trends in Graphene Grain Boundaries. *Phys. Rev. B* **2010**, *81*, 165447.

(16) Salehi-Khojin, A.; Estrada, D.; Lin, K. Y.; Bae, M.; Xiong, F.; Pop, E.; Masel, R. I. Polycrystalline Graphene Ribbons as Chemiresistors. *Adv. Mater.* **2012**, *24*, 53-57.

(17) Zhang, Y.; Brar, V. W.; Wang, F.; Girit, C.; Yayon, Y.; Panlasigui, M.; Zettl, A.; Crommie, M. F. Giant Phonon-Induced Conductance in Scanning Tunnelling Spectroscopy of Gate-Tunable Graphene. *Nat. Phys.* **2008**, *4*, 627-630.

(18) Yazyev, O. V.; Louie, S. G. Topological Defects in Graphene: Dislocations and Grain Boundaries. *Phys. Rev. B* **2010**, *81*, 195420.

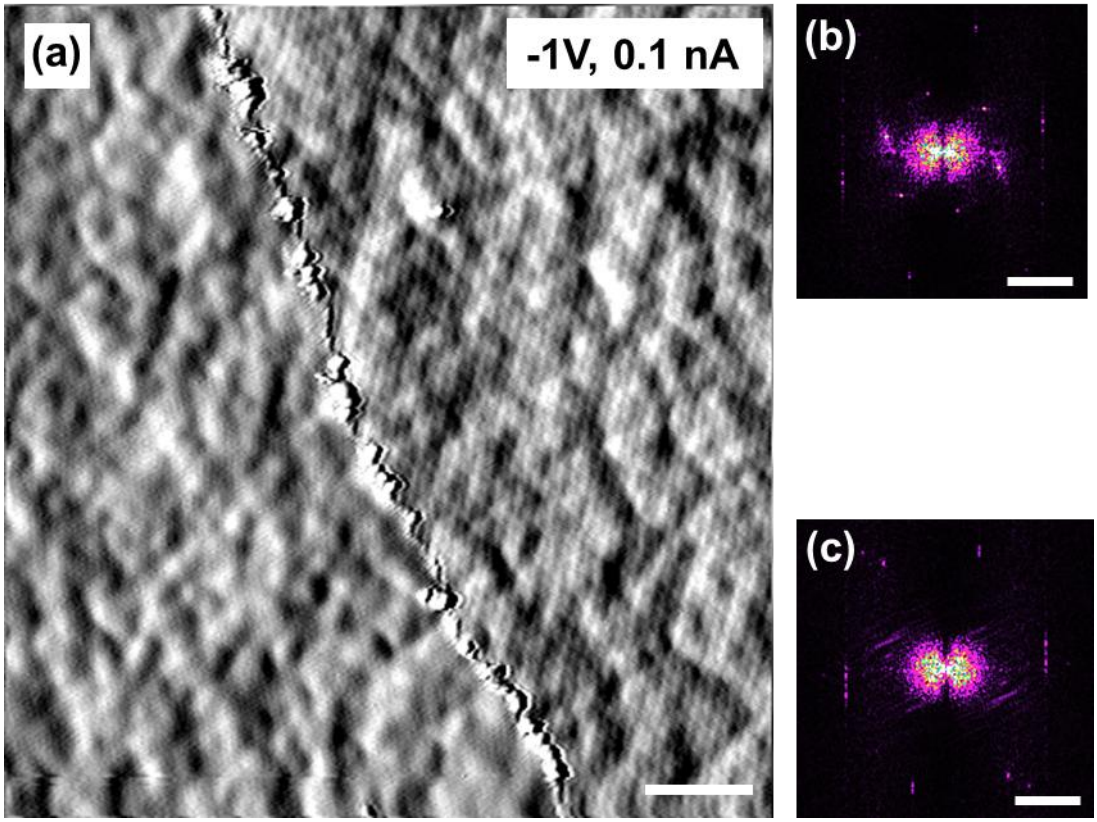

Figure S1. Moiré patterns. (a) This large 71.5 nm x 75.6 nm STM scan shows two different Moiré patterns on either side of a grain boundary (GB). The misorientation angle between the two graphene grains is ~29°. The scale bar is 10 nm. (b) FFT of the upper-right region of the scan shown in (a). The scale bar is 1 nm^{-1}. (c) FFT of the lower-left region of the scan shown in (a) also with a 1 nm^{-1} scale bar. The FFTs show the presence of two different Moiré patterns on either side of the GB rotated with respect to one another by ~29°. The Moiré pattern in (c) is also stretched in one direction indicating some possible strain in the Moiré pattern.

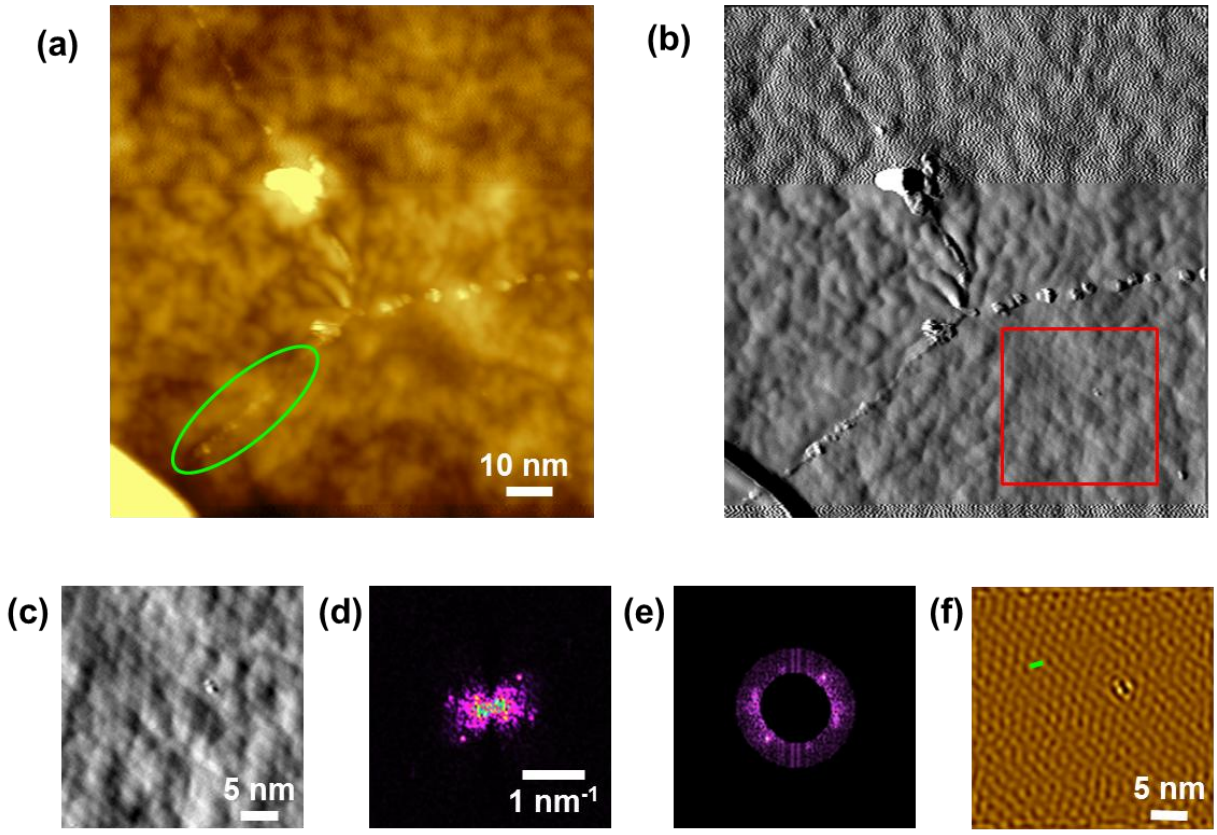

Figure S2. Moiré pattern adjacent to grain boundary. (a) Larger 102.7 nm x 108.7 nm STM topograph of area adjacent to GB shown in main Figure 6. The green ellipse highlights the GB from main Figure 6. (b) Topographic derivative of illustrating Moiré pattern in lower-right section of the scan. (c) Smaller region of (b) as highlighted by the red box in (b) showing the Moiré pattern more clearly. (d) FFT of region shown in (c). (e) Filter mask from (d) used to extract the Moiré pattern. (f) Filtered version (c) created using the filter mask shown in (e). The period of the Moiré pattern is ~1.5 – 1.65 nm. Thus the top layer and bottom layer of graphene in the region highlighted by the red box in (b) are misoriented by ~8.5 – 9.5°.

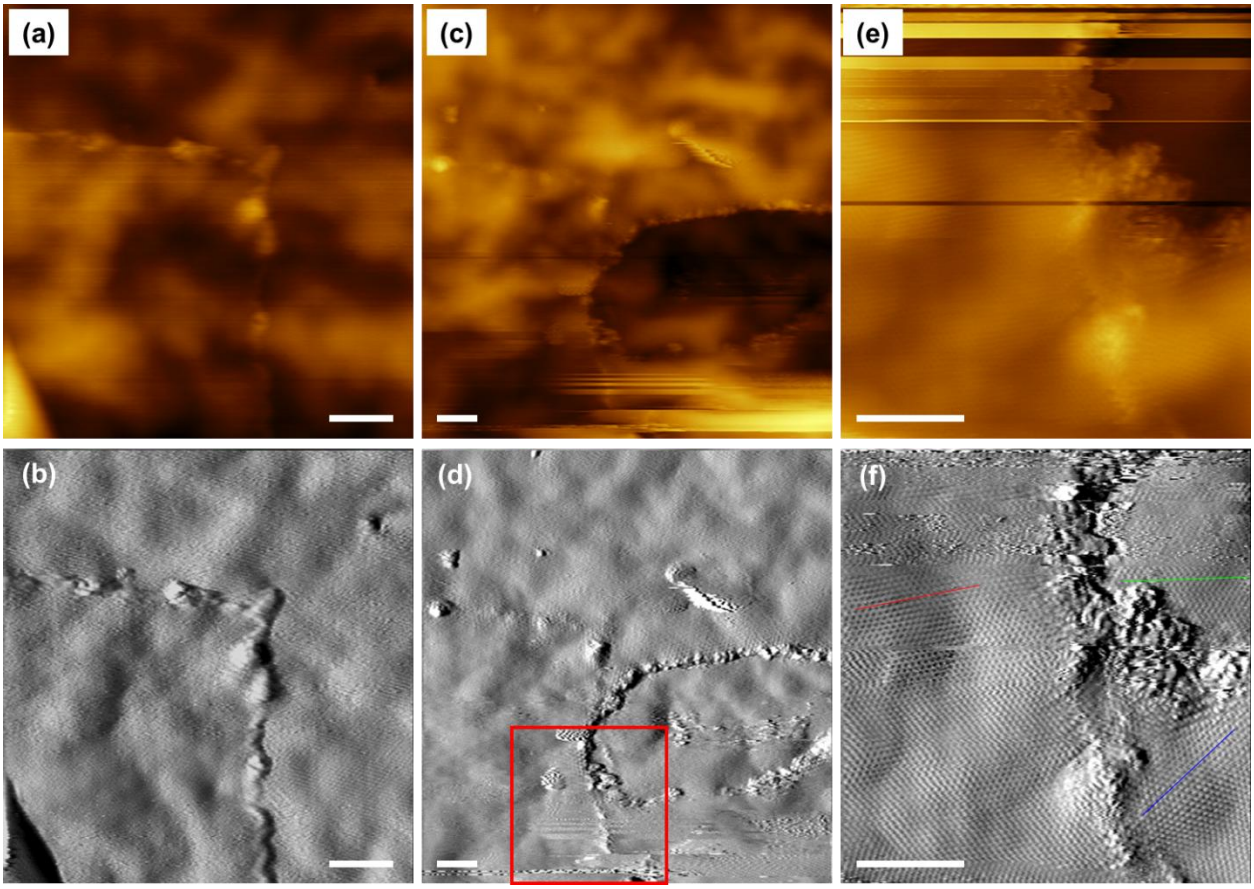

Figure S3. Ripped graphene section. The scale bars are 4 nm. (a) An STM topograph of a grain boundary (GB) making a right angle on the surface before a tip destabilization. (b) Derivative of the STM topograph from (a) for better contrast of the GB. (c) STM topograph of the same area as (a) and (b) after a strong tip-surface interaction ripped a section of graphene out of the top layer of the bilayer graphene starting at the GB. (d) Derivative of the STM topograph from (c) for better contrast. (e) Smaller STM topograph of approximately the area outlined by the red box in (d) after the rip. (f) Derivative of the STM topograph from (e) with colored lines indicating one of the local zigzag directions of the graphene lattice illustrating the relative rotational misorientation of the left and right graphene grains of the top layer with the bottom layer of graphene.

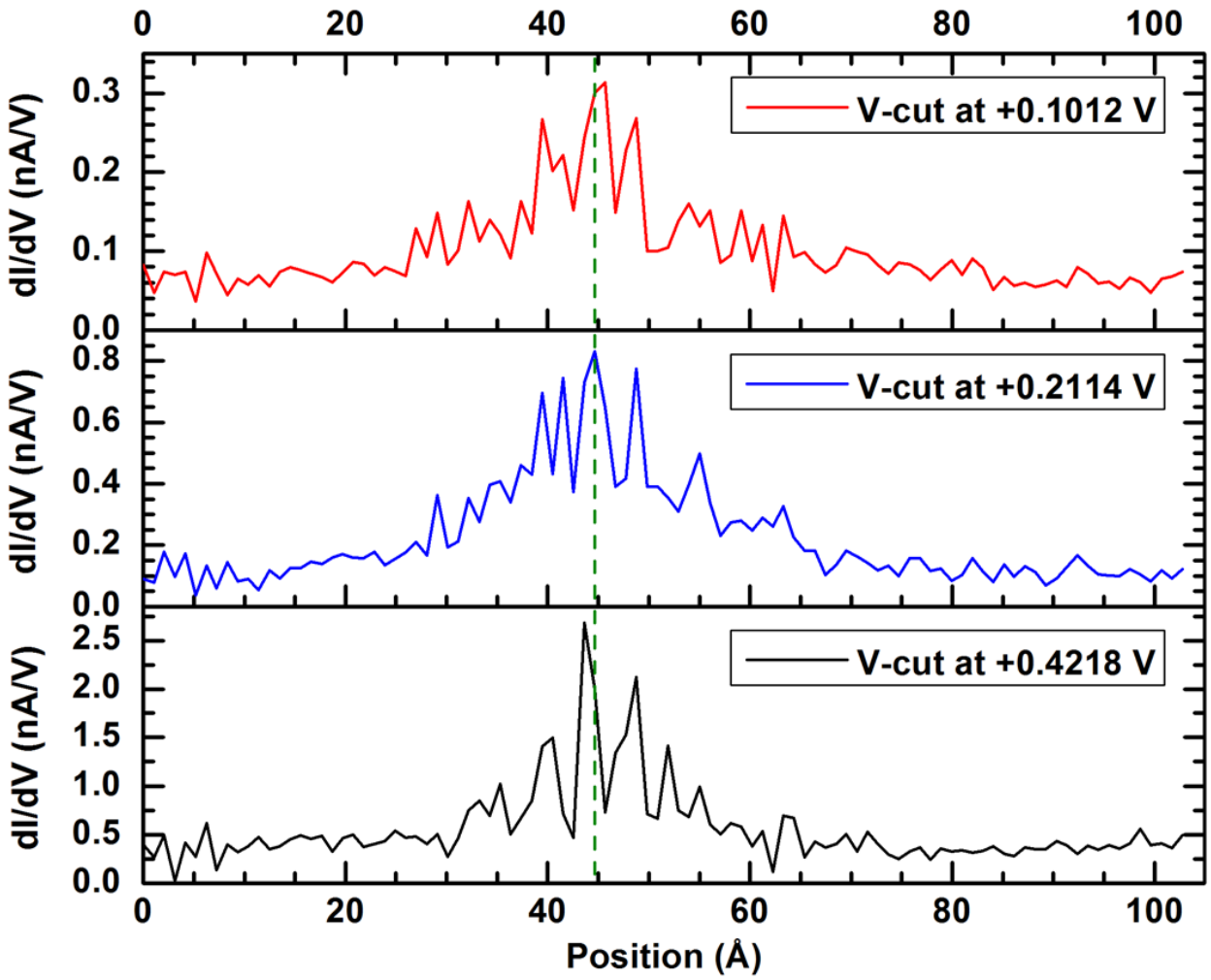

Figure S4. Voltage cuts of dI/dV spectra map. The three plots show cuts of the (*dI*/*dV*) spectra map from Figure 3e at three different tip-sample biases illustrating the enhanced tunneling conductance present at the GBs in empty states. The dashed, vertical green line in the plots indicates the lateral position of the GB.

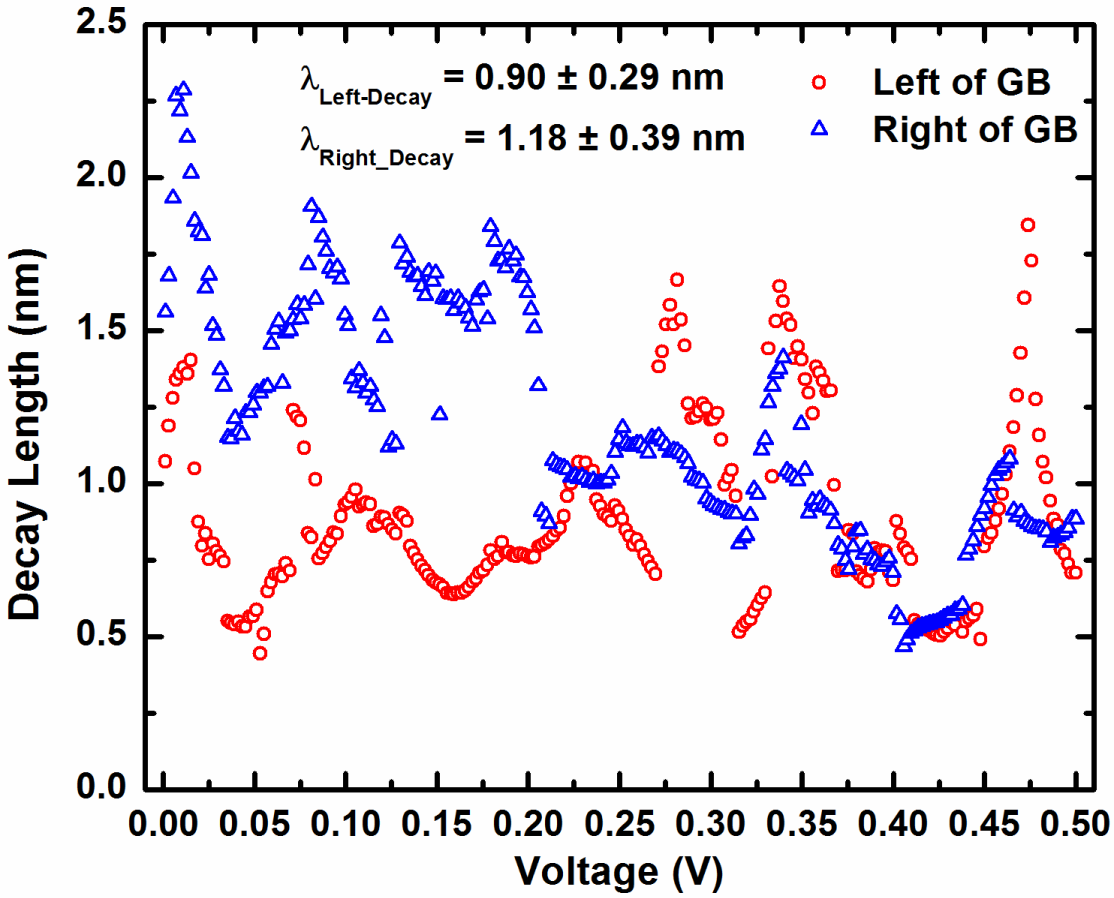

Figure S5. Decay length of enhanced empty states tunneling conductance at a grain boundary (GB), extracted from the spectra map in Figure 3e as a function of the tip-sample bias. The blue circles indicate the decay lengths to the left of the GB, whereas the red ones indicate the decay lengths to the right of the GB. The average decay length on the left side of the GB (shown in Figure 3d) is 0.90 ± 0.29 nm, and the average decay length on the right side of the GB is 1.18 ± 0.39 nm. These decay lengths suggest that the perturbation to the graphene from the GB decays on the order or 1 nm. The asymmetric decay length likely results from having different edge structure of the graphene lattice where the defects at the GB start.

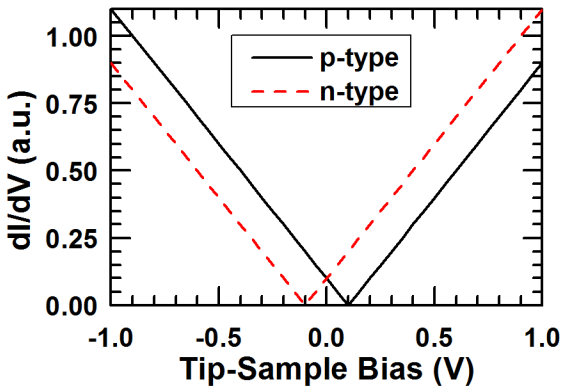

Figure S6. Illustration of effect of graphene doping shift on tunneling conductance. The plot shows the ideal graphene DOS for p-type doping (solid, black curve) and for n-type doping (dashed, red curve). This plot illustrates that a region with n-type doping, or even lower concentration p-type doping than the bulk would have enhanced empty states tunneling conductance compared to the surrounding regions.

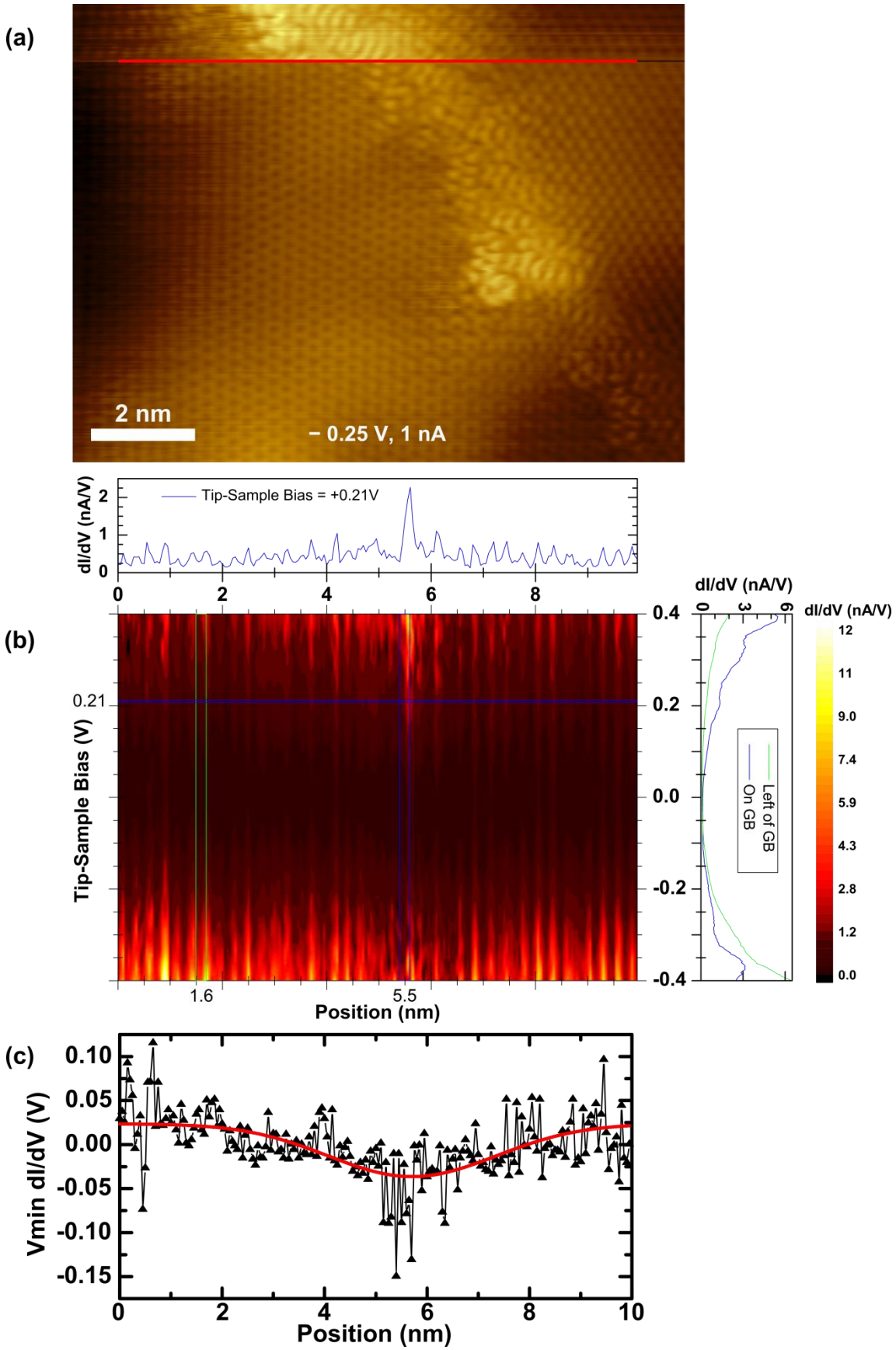
(a)
2 nm
– 0.25 V, 1 nA
(b)
Tip-Sample Bias = +0.21V
dI/dV (nA/V)
Tip-Sample Bias (V)
0.21
Position (nm)
1.6
5.5
Left of GB
On GB
(c)
Vmin dI/dV (V)
Position (nm)

Figure S7. Large angle graphene grain boundary (GB) spectroscopy on mica. (a) An STM topograph of a large angle graphene GB on mica with a grain misorientation angle of ~29°. The scale bar is 2nm, and the red line indicates the location of a line of tunneling spectroscopy points. (b) Map of tunneling conductance as a function of tip-sample bias and position along line indicated in (a). The spectra map shows enhanced empty states *(dI/dV)* near the location of the GB. The blue, horizontal line indicates the location of a constant tip-sample bias cut displayed in plot above the spectra map, showing locally enhanced *(dI/dV)* at the GB. The pairs of vertical lines on the spectra map indicate the location of representative off and on GB *(dI/dV)* curves displayed in the plot to the right of the spectra map. (c) Plot of the tip-sample bias of the minimum value of each *(dI/dV)* spectra from the line indicated in (a) *versus* position, showing the shift of the tip-sample bias of the *(dI/dV)* minimum at the GB. This GB occurs in a region of bilayer graphene.

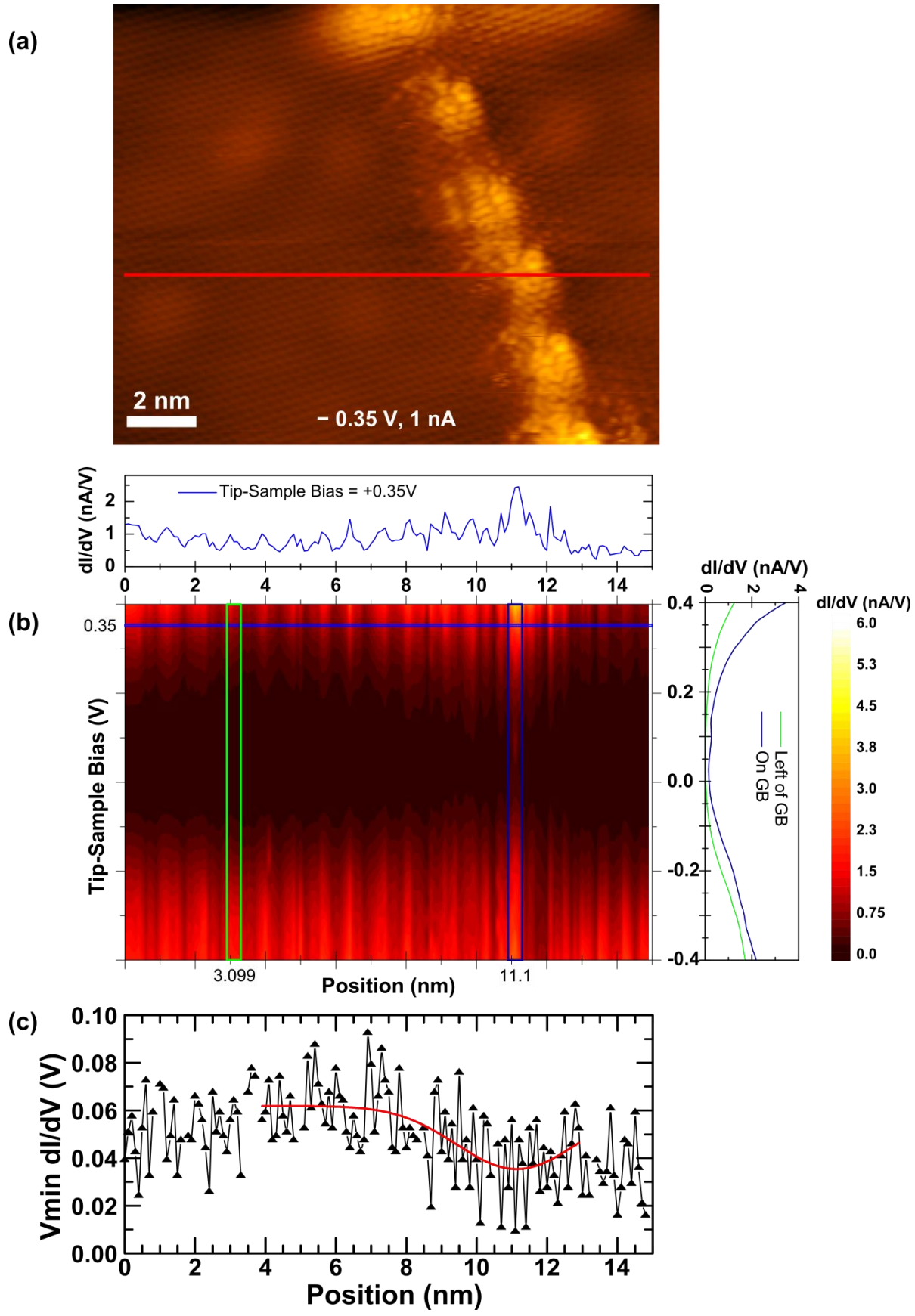
(a)
2 nm
− 0.35 V, 1 nA
(b)
Tip-Sample Bias = +0.35V
dI/dV (nA/V)
Tip-Sample Bias (V)
Position (nm)
3.099
11.1
Left of GB
On GB
(c)
Vmin dI/dV (V)
Position (nm)

Figure S8. Small angle graphene grain boundary (GB) spectroscopy on mica. (a) An STM topograph of a small angle graphene GB on mica with a grain misorientation angle of ~6°. The scale bar is 2nm, and the red line indicates the location of a line of tunneling spectroscopy points. (b) Map of tunneling conductance as a function of tip-sample bias and position along line indicated in (a). This spectra map also shows enhanced empty states *(dI/dV)* near the location of the GB. The plot above the spectra map shows a constant tip-sample bias cut of the spectra map from the location of the horizontal, blue line and shows locally enhanced empty states *(dI/dV)* at the GB. The plot to the right of the spectra map shows a comparison of representative on and off GB *(dI/dV)* curves taken from the locations indicated by the vertical lines on the spectra map. (c) Plot of the tip-sample bias of the minimum value of each *(dI/dV)* spectra from the line indicated in (a) *versus* position. The red curve is an attempted Gaussian fit to part of the data. However, the shift due to the GB is smaller than the shift from the left graphene grain to the right graphene grain.

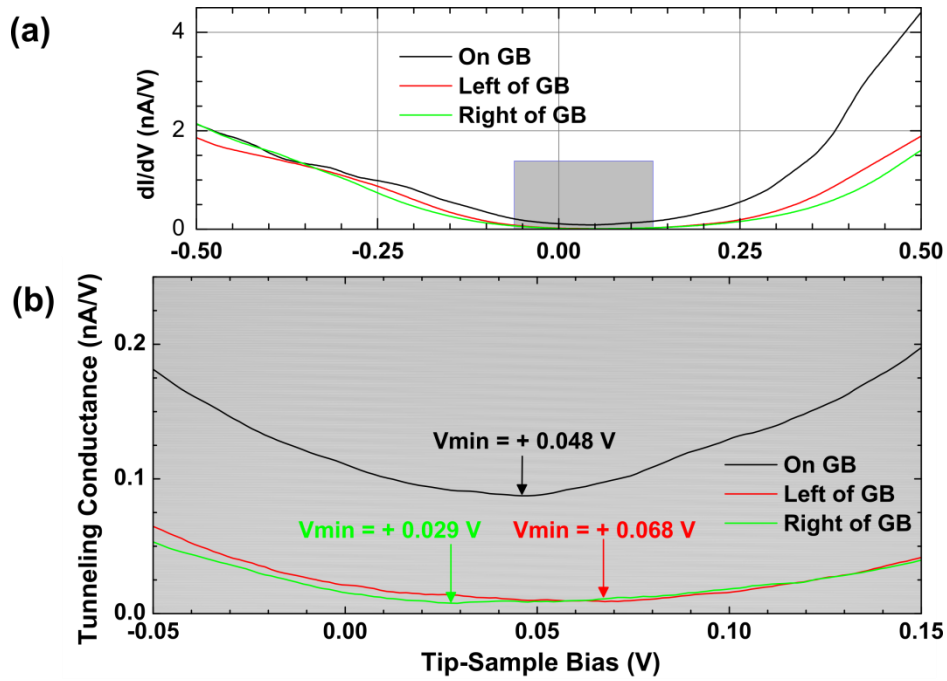

Figure S9. Small angle graphene grain boundary (GB) on and off GB tunneling conductance comparison. (a) Plot of the average tunneling conductance from left side, right side, and on the GB from Figure S8. (b) Magnified small tip-sample bias section of (a) showing tip-sample biases of the minima of the average *(dI/dV)* to the left, to the right, and on the GB.

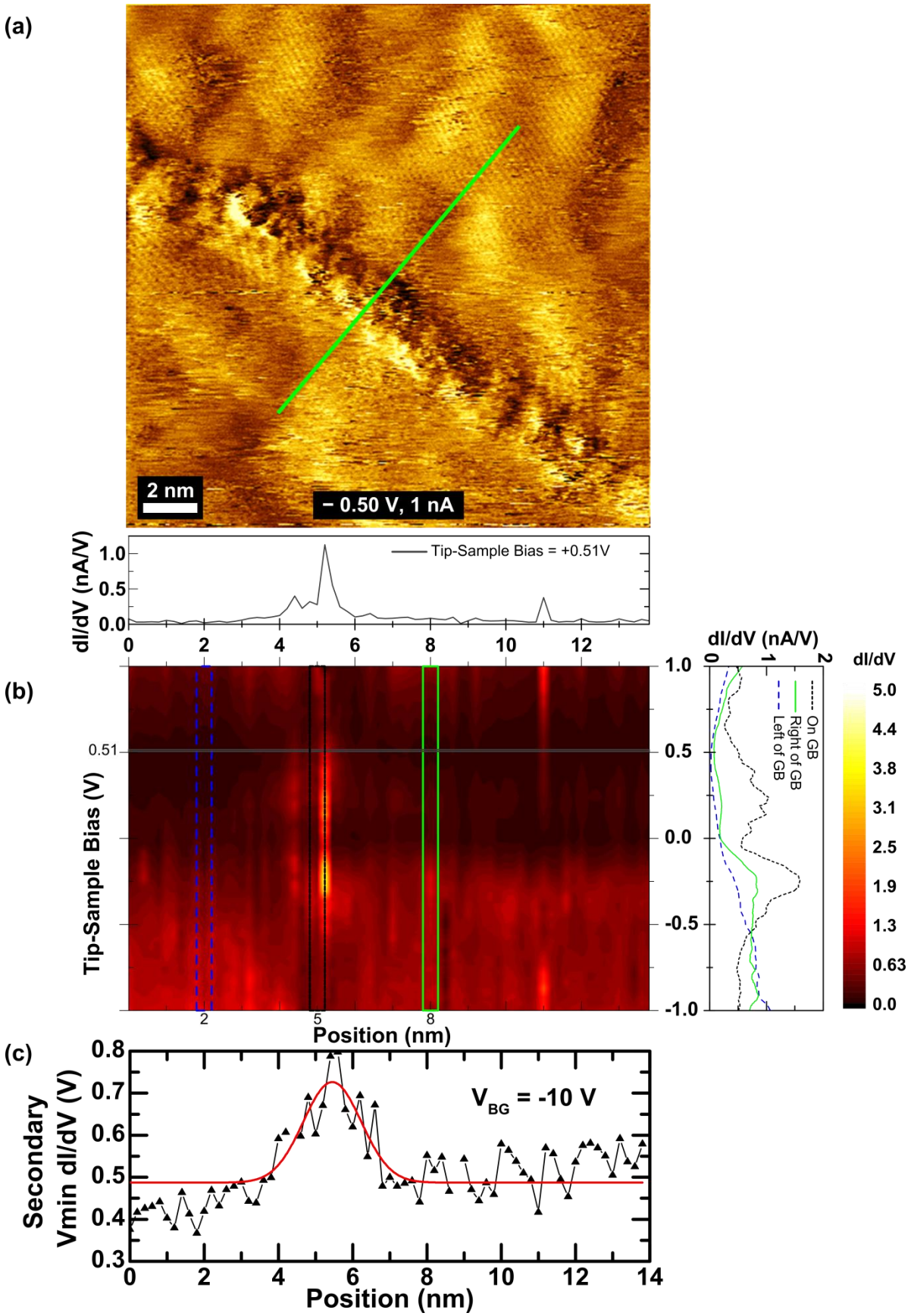
(a)
2 nm
– 0.50 V, 1 nA
dI/dV (nA/V)
Tip-Sample Bias = +0.51V
(b)
Tip-Sample Bias (V)
0.51
Position (nm)
dI/dV (nA/V)
On GB
Right of GB
Left of GB
dI/dV
(c)
Secondary Vmin dI/dV (V)
V_BG = -10 V
Position (nm)

Figure S10. Tunneling spectroscopy of back-gated CVD graphene grain boundary (GB): V_{BG} = −10V. (a) STM image of a back-gated GB on SiO_2/Si with a grain misorientation angle of ~12°. The scale bar is 2 nm, and the green line indicates the location of a line of tunneling spectra points. (b) Map of tunneling conductance as a function of tip-sample bias and position along line indicated in (a). This spectra map shows enhanced filled and empty states *(dI/dV)* near the location of the GB. The plot above the spectra map shows a constant tip-sample bias cut of the spectra map from the location of the horizontal, gray line and shows locally enhanced filled and empty states *(dI/dV)* at the GB. The plot to the right of the spectra map shows a comparison of representative on and off GB *(dI/dV)* curves taken from the locations indicated by the vertical lines on the spectra map. (c) Plot of the tip-sample bias of the secondary minimum value of each *(dI/dV)* spectra from the line indicated in (a) *versus* position. The red curve is a Gaussian fit to part of the data, showing the shift in the tip-sample bias of the secondary *(dI/dV)* minima due to the GB.

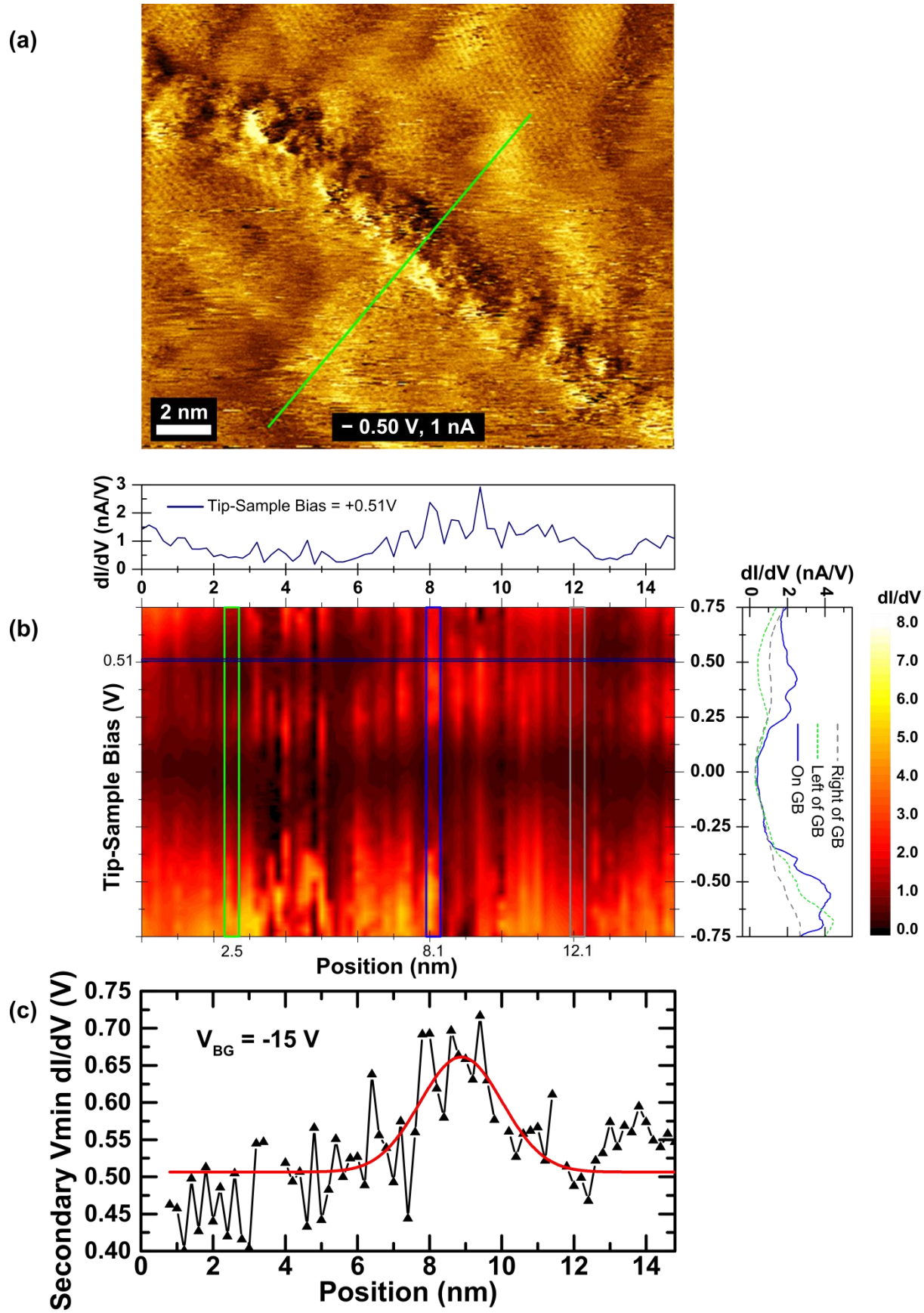
(a)
2 nm
− 0.50 V, 1 nA
(b)
dI/dV (nA/V)
Tip-Sample Bias = +0.51V
Tip-Sample Bias (V)
0.51
Position (nm)
2.5
8.1
12.1
dI/dV (nA/V)
Right of GB
Left of GB
On GB
dI/dV
(c)
Secondary Vmin dI/dV (V)
V_BG = -15 V
Position (nm)

Figure S11. Tunneling spectroscopy of back-gated CVD graphene grain boundary (GB): V_{BG} = −15V. (a) STM image of the same back-gated GB from Figure S10 on SiO_2/Si with a grain misorientation angle of ~12°. The scale bar is 2 nm, and the green line indicates the location of a line of tunneling spectra points. (b) Map of tunneling conductance as a function of tip-sample bias and position along line indicated in (a). This spectra map shows slightly enhanced empty states *(dI/dV)* near the location of the GB. The plot above the spectra map shows a constant tip-sample bias cut of the spectra map from the location of the horizontal, blue line and shows locally enhanced filled and empty states *(dI/dV)* at the GB. The plot to the right of the spectra map shows a comparison of representative on and off GB *(dI/dV)* curves taken from the locations indicated by the vertical lines on the spectra map. (c) Plot of the tip-sample bias of the secondary minimum value of each *(dI/dV)* spectra from the line indicated in (a) *versus* position. The red curve is a Gaussian fit to part of the data, showing the shift in the tip-sample bias of the secondary *(dI/dV)* minima due to the GB.

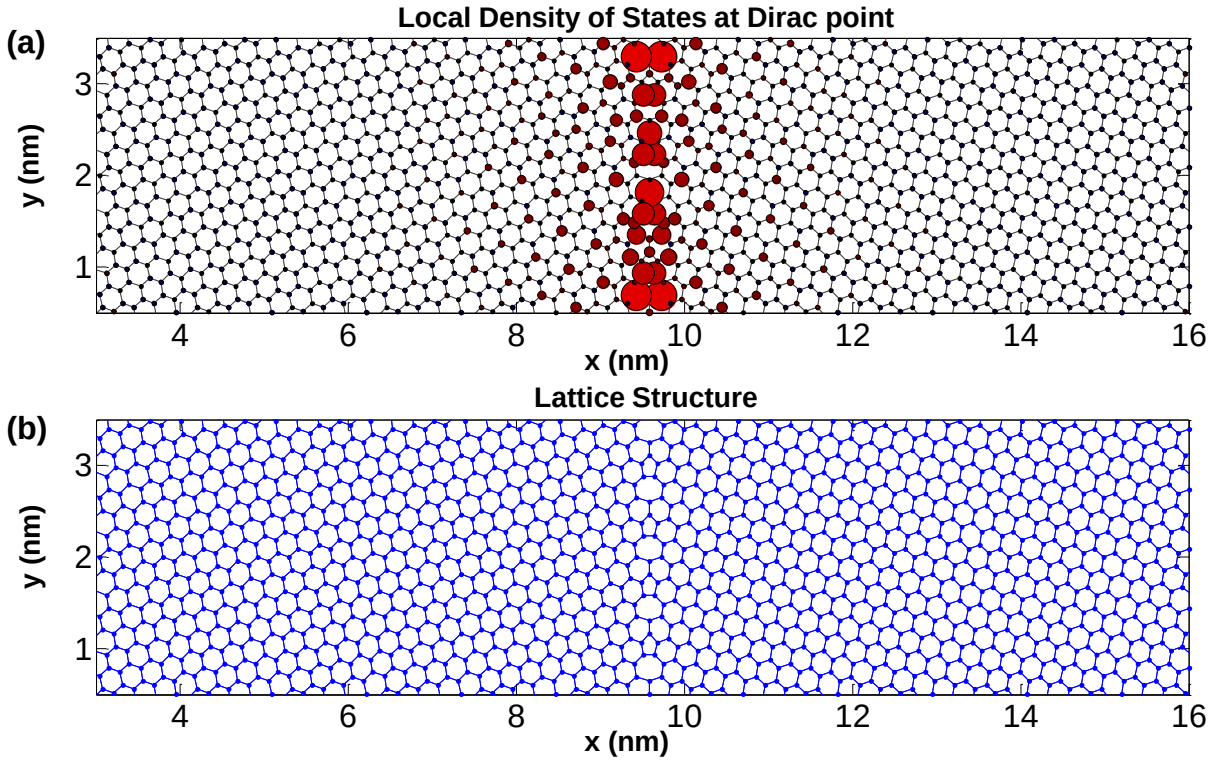

Figure S12. Tight-binding simulation of a grain boundary (GB). (a) A plot of the local density of states at the Dirac point showing a predominantly $\left(\sqrt{3}\times\sqrt{3}\right)R30°$ superstructure caused by the presence of the GB. (b) Physical lattice structure of the graphene and the GB used in the tight-binding calculation to obtain (a).